***Snrpb*, the gene mutated in CCMS, is haploinsufficient and required for proper morphogenesis and splicing**

Sabrina Shameen Alam[1,2], Shruti Kumar[1,2], Marie-Claude Beauchamp [1], Eric Bareke [2], Alexia Boucher[1,3], Nadine Nzirorera[1,2], Reinnier Padilla[2], Si Jing Zhang[2], Jacek Majewski[2], Loydie A. Jerome-Majewska [1,2,3,4*]

[1] Research Institute of the McGill University Health Centre at Glen Site, Montreal, QC, H4A 3J1, Canada

[2] Department of Human Genetics, McGill University, Montreal, QC, H3A 0G1, Canada

[3] Department of Anatomy and Cell Biology, McGill University, Montreal, QC, H3A 2B2, Canada

[4]Department of Pediatrics, McGill University, Montreal, QC, H4A 3J1, Canada

*Correspondence: loydie.majewska@mcgill.ca

Summary:

Heterozygous mutations in *SNRPB*, an essential core component of the five small ribonucleoprotein particles of the spliceosome, are responsible for craniofacial and rib defects in patients with Cerebrocostomandibular Syndrome. We show a conserved role for *Snrpb* in morphogenesis of the rib and head in a mouse line heterozygous for a 61-base pair intronic deletion that perturbed splicing of a pretermination codon containing exon. In addition, deletion of *Snrpb* in the developing brain and neural crest, led to malformations, and death of heterozygous embryos. Furthermore, though splicing of *Mdm2* and *Mdm4*, and levels of P53-pathway genes were increased in mutants, craniofacial defects were not fully rescued when P53 was deleted. We propose that abnormal splicing of P53 regulatory genes and genes important for craniofacial development, including the transcription factors *Smad2* and *Rere* together lead to apoptosis of *Snrpb* mutant cells and craniofacial malformations in CCMS.

Keywords: Cerebrocostomandibular syndrome (CCMS); *SNRPB*; splicing; neural crest cells (NCCs); craniofacial

INTRODUCTION

95% of human pre-mRNAs are alternatively spliced to generate multiple mRNAs (Chen and Manley, 2009; Nilsen and Graveley, 2010) thus increasing the number and diversity of proteins found in the human genome. The major spliceosome or U2-dependent spliceosome catalyses 99% of RNA splicing reactions in human (Wickramasinghe *et al*., 2015), while the minor or U12-dependent spliceosome is responsible for splicing of approximately 700 minor introns in 666 genes (Olthof *et al.*, 2019). The major spliceosome is composed of U1, U2, U5, and U4/U6 small nuclear ribonucleoprotein proteins (snRNPs) named for their core associated small RNAs (snRNAs). *SNRPB* encodes for SmB and SmB' which are core components of the spliceosome. SmB/B' helps to form the heptameric ring on the U snRNAs of the five snRNPs of the major spliceosome. Several groups have reported heterozygous mutations in *SNRPB* in patients with Cerebrocostomandibular Syndrome (CCMS, OMIM# 117650) (Lynch *et al.*, 2014, Barcot *et al.*, 2015, Tooley *et al.*, 2016). CCMS patients have rib gaps and narrow chests, and craniofacial defects such as malar hypoplasia and micrognathia, with variable expressivity (Beauchamp *et al*., 2020). Furthermore, *SNRPB* mutations show incomplete penetrance.

In addition to the two coding transcripts, SmB and SmB', *SNRPB* also encodes for a third premature termination codon (PTC) containing transcript that is predicted to undergo non-sense mediated decay. Most of the mutations found in CCMS patients increase inclusion of the PTC containing alternative exon 2 leading to no change or reduced levels of the coding transcripts in patient's fibroblasts (Barcot *et al.*, 2015 and Lynch *et al.* 2014). However, though it is presumed that increased expression of the PTC-containing transcript leads to reduced level of SmB/SmB' in all CCMS patients, reduced levels of SNRPB protein has not been reported in any CCMS patient cells. Also, the question of why mutation of a ubiquitous core splicing factor like *SNRPB* leads to the tissue specific abnormalities found in CCMS patients remains unanswered. We postulated that a mouse model with a mutation in *Snrpb* can be used to understand the role of *Snrpb* during embryogenesis and to shed insight into the etiology of CCMS.

Towards this goal, we generated two mutant mouse models with distinct mutations in *Snrpb*. Using the first model we show that an intronic deletion of 61 base pairs increased

inclusion of the mouse PTC-containing exon 2 and resulted in craniofacial, rib and limb defects in embryos and pups, and reduced survival during adulthood. In the second model, we flanked the genomic region that encompasses exons 2 and 3 with loxp sequences to make a conditional mutant mouse line. Using β-actin-cre we showed that widespread heterozygous deletion (*Snrpb*$^{+/-}$) of this region reduced levels of *Snrpb* and resulted in embryonic arrest by embryonic (E) 9.5. To investigate the role of *Snrpb* specifically during craniofacial development, we used *Wnt1-Cre2* to generate heterozygous mutant embryos with deletion of *Snrpb* in the developing brain and neural crest cells (*Snrpb*$^{ncc+/-}$). We showed that a small subset of these embryos survived to birth and die shortly after. Most *Snrpb*$^{ncc+/-}$ mutant embryos die between E17.5 and birth, with brain and craniofacial defects of variable expressivity. RNAseq analysis of the developing head of *Snrpb*$^{ncc+/-}$ embryos, before morphological defects were apparent, revealed few differentially expressed genes (DEGs) in these embryos. Pathway analysis indicated that these DEGs were associated with the spliceosome and the P53-pathway. In contrast, a large number of transcripts, including several important for craniofacial development, were differentially spliced, and these transcripts were significantly associated with mRNA processing. Furthermore, *Snrpb*$^{ncc+/-}$ mutants had increased expression of core spliceosome and P53-downstream pathway genes. However, although nuclear P53 and apoptosis were increased in *Snrpb*$^{ncc+/-}$ embryos, reducing levels of P53 genetically in the neural crest did not rescue craniofacial defects in these mutants. Our findings support disrupted splicing as the major driver of abnormalities in *Snrpb* mutant embryos and show that mutation in mouse *Snrpb* results in variable expressivity at both the molecular and phenotypic levels.

RESULTS

A 61 bp intronic deletion of *Snrpb* regulates inclusion of alternative exon2 and models CCMS at a low penetrance

To generate a conditional mutant mouse model that can be used to reduce levels of *Snrpb* and uncover its role during rib and craniofacial development, we used CRISPR/Cas9 to insert loxP sequences in the *Snrpb* genomic locus. When trying to insert loxP sequences in intron 2 of mouse *Snrpb,* we recovered a mutant mouse line with a 61bp intronic deletion (Δ61) upstream of the alternatively spliced exon 2 (Figure S1A). We noted that a subset of Δ61 heterozygous

embryos was abnormal at birth. Morphological examination of embryos and pups crossed to wild type CD1 for at least 5-generation from the initial CRISPR/Cas9 founder revealed that a significant proportion of Δ61 heterozygous (n=15/306) and homozygous (n=11/168) mutant embryos were abnormal (Figure 1A, and S1 B-G) when compared to wild types (n=160) (T-test, p=.007).

To examine cartilage and bone formation in embryos from the Δ61 line, embryonic day (E) 14.5 and E17.5 embryos were used for Alcian blue and Alizarin red staining, respectively. These experiments revealed craniofacial, ribs and/or limb defects in 6% of *Snrpb*$^{\Delta 61/+}$ and 23% of *Snrpb*$^{\Delta 61/\Delta 61}$ embryos. Malformations ranged from a complete absence of cartilage derivatives in the head and ventral ribs (Figure 1B) to the presence of an extra pair of ribs (n=2/8) and finger defects (n=5/43) such as polydactyly and clinodactyly (Figure S1D-S1F). Additionally, *Snrpb*$^{\Delta 61/+}$ and *Snrpb*$^{\Delta 61/\Delta 61}$ pups were smaller than their wild type littermates from birth and this difference became significant from 6 to 48 weeks (data not shown). Moreover, a significant proportion of heterozygous and homozygous mutants died or had to be euthanized between 4 and 48 weeks of life, suggesting that this mutation reduced fitness (Figure S1H). Thus, we concluded that *Snrpb* has a conserved requirement during development of structures affected in CCMS patients, mainly the ribs and craniofacial region. We also uncovered a postnatal requirement for *Snrpb*.

We postulated that the Δ61 deletion increases inclusion of the PTC containing exon 2 thereby reducing levels of *Snrpb*. RT-PCR analyses showed a non-significant increase in the proportion of E11.5 *Snrpb*$^{\Delta 61/+}$ (3/3) and *Snrpb*$^{\Delta 61/\Delta 61}$ (2/4) mutant embryos with inclusion of alternative exon 2, when compared to wild type (n=1/4) (Figure S1I). In addition, western blot analysis revealed a non-significant reduction in SNRPB levels in *Snrpb*$^{\Delta 61/+}$ and *Snrpb*$^{\Delta 61/\Delta 61}$ mutant embryos (Figure S1J and S1K). Altogether, these findings show a correlation between increased inclusion of the PTC containing exon 2 and a non-significant reduction of SNRPB protein in embryos from the Δ61 line. Hence, the 61 bp deletion removes or disrupts regulatory sequences that control inclusion of the conserved PTC containing exon 2. However, the low penetrance of this deletion made it difficult to use the *Snrpb* Δ61 line to study the role of *Snrpb* in rib and craniofacial development.

***Snrpb* heterozygous (*Snrpb*$^{+/-}$) embryos die before the organogenesis**

Since we found that intron 2 contained regulatory sequences important for inclusion of exon 2, we instead inserted loxP sites into intron 1 and intron 3, to flank the region that encompasses exon 2, the PTC encoding alternative exon 2, and exon 3 of *Snrpb* (*Snrpb*$^{loxp/+}$) (Figure S2A). We first mated *Snrpb*$^{loxp/+}$ mice with β-actin-cre transgenic mice to produce heterozygous (*Snrpb*$^{+/-}$) offspring with widespread deletion of *Snrpb*. However, no *Snrpb*$^{+/-}$ mice were found at birth (P0) or at weaning, indicating that these mutants died before birth (data not shown). To determine when *Snrpb*$^{+/-}$ embryos die, we dissected pregnant females from E6.5 – E10.5 and found that mutant embryos were undergoing resorption by E9.5 (data not shown). We show that *Cre*-mediated deletion of the loxp flanked region generated a shorter *Snrpb* transcript of 527 bp (Figure S2B), and resulted in a statistically significant 70% reduction in levels of *Snrpb* in E8.5 *Snrpb*$^{+/-}$ embryos (p= 0.0052, T-Test) (Figure S2C). Thus, deletion of exons 2 – 3 of *Snrpb* leads to a significant reduction in *Snrpb* level in heterozygous mutant embryos. Our data indicate that the amount of functional protein made by the single wild type allele of *Snrpb* is insufficient for embryonic growth and survival post-implantation. These data also confirm our findings from the Δ61 line that *Snrpb* is haploinsufficient.

Snrpb heterozygosity in neural crest cells causes abnormal brain and craniofacial development and results in postnatal death

To examine the conserved role of *Snrpb* in craniofacial development, we used *Wnt1-Cre2* to delete *Snrpb* in the neural tube and neural crest cells. *Snrpb*$^{loxp/+}$ and *Wnt1-Cre2* transgenic mice were mated to generate *Snrpb* heterozygous mice (*Snrpb*$^{ncc+/-}$) with deletion of exons 2 -3 in the developing brain and in neural crest cells (Figure S3A). We found no *Snrpb*$^{ncc+/-}$ mutant pups at P1 and P21 (p>.0001, chi-square), a significant deviation from the expected Mendelian ratio. However, 5 heterozygous mutants were recovered at P0 indicating that *Snrpb*$^{ncc+/-}$ mutant pups can be born but do not survive to weaning (See SI4). In addition, P0 *Snrpb*$^{ncc+/-}$ mutants were phenotypically abnormal with no visible milk spots, indicating that they failed to feed (n=4/5). These mutant embryos had abnormally shaped heads and small outer ears (Figure S3B-S3F). Furthermore, skeletal preparations revealed palatine defects in *Snrpb*$^{ncc+/-}$ mutant (n=3/3). Two mutants showed clefts in the premaxilla and missing palate (Figure S3G) while the palatal process of the premaxilla of the third was abnormally curved. The basisphenoid, and squamous bones were hypoplastic and the temporal bone was also abnormal (Figure S3G). In addition,

Meckel's cartilage and the lower jaw which forms around it were asymmetric and abnormal in all three mutants. Specifically, in one mutant, the condyloid and the angular processes were shortened bilaterally, while only the angular process was asymmetrically affected in the other two mutants (Fig S3H) We also saw middle ear defects such as absent, or abnormally shaped tympanic ring, and presence of ectopic ossification in these heterozygous mutants (Figure S3I). Because *Snrpb*$^{ncc+/-}$ pups have not been found alive at P1 or P21 (n= 0/78) (p>.0001, chi-square test), we concluded that palatal and skull defects lead to death of *Snrpb*$^{ncc+/-}$ pups that are born.

To uncover when *Snrpb* is first required in neural crest cells we collected embryos between E9.0 and E17.5 for morphological analysis, and for micro-CT and skeletal preparations from E12.5 – E17.5. *Snrpb*$^{ncc+/-}$ mutants were found at the expected Mendelian ratio until P0, approximately, 30% of heterozygous embryos were dead at E14.5, and E17.5 (See SI3). At E9.0, *Snrpb*$^{ncc+/-}$ embryos with thirteen somites or less, were indistinguishable from wild type controls (Figure S4A). Morphological abnormalities were first apparent at E9.5, where 48% of *Snrpb*$^{ncc+/-}$ embryos exhibited hypoplasia of their hindbrain, midbrain, forebrain, frontonasal prominence, and pharyngeal arches. From E10.5 onwards, the majority of *Snrpb*$^{ncc+/-}$ embryos (>80%) were morphologically distinguishable from wild type and control littermates. At E10.5, abnormal heterozygous mutant embryos showed hypoplasia of the craniofacial region, like what was found at E9.5 (Figure S4C). At E11.5, abnormal *Snrpb*$^{ncc+/-}$ embryos could be sorted into three groups: group 1 were indistinguishable from wild type, group 2 exhibited hypoplasia of the developing face and head, and those in group 3 lacked the frontonasal and maxillary prominences, and had an extremely hypoplastic mandibular arch (Figure S4D). At E12.5, *Snrpb*$^{ncc+/-}$ embryos could be sorted into four groups. Those in group 1 were normal, heterozygous mutant embryos in group 2 showed cleft of the frontonasal region and the jaw, while those in group 3 had very little tissue ventral to the eye but had distinguishable frontonasal and maxillary tissues that failed to fuse at the midline (Figure S4E). *Snrpb*$^{ncc+/-}$ embryos in group 4 were the most severe found at this stage and showed a complete absence of the ventral portion of the head and face, edema in the head, and a hypoplastic mandibular arch (Figure S4E right panel). At E14.5 and E17.5, morphologically normal *Snrpb*$^{ncc+/-}$ embryos were no longer found. Mutant embryos in group 2 had hypoplastic pinna, dome-shaped heads, abnormal eyes, and nasal clefts at E14.5 but, only a smaller abnormally shaped outer ear at E17.5. Those in group 3 showed hypoplasia and cleft of the frontonasal, maxilla and mandibular regions, eye anomalies and edema (Figure 1C and 1D).

At E14.5 and E17.5, *Snrpb*$^{ncc+/-}$ embryos in group 4 were the most severe and exhibited exencephaly with no defined structures of the head and face (Figure 1C and 1D). Thus, *Snrpb* is essential in neural crest cells from E9.5 onwards for normal development of the head and face.

We examined the formation of neural crest-derived cartilage and bones in *Snrpb*$^{ncc+/-}$ mutants at E14.5 and E17.5 and found severe abnormalities with variable expressivity (Figure 2A, SI 1A). Mutant embryos in groups 2 and 3 showed hypoplasia of the mesoderm-derived parietal bone (n=8), missing or reduced ossification of the neural crest-derived frontal, alisphenoid and squamous bones, and hypoplasia of the intraparietal bone, which forms from both neural crest and mesoderm (n= 5) (Figure 2B, SI1). Mutant embryos in these two groups also showed clefts of the nasal and pre-maxillary cartilages and bones, the palate, as well as hypoplasia of Meckel's cartilage and its derivative, the lower jaw (Figure 2C, 2D and SI1). In addition, at both stages, heterozygous mutant embryos in group 4 had none of the neural crest cell-derived cartilage or bone elements normally found on the ventral surface of the head and face, and the basisphenoid bone was hypoplastic (Figure 2B and SI1)while the zygomatic arch failed to form in group 3 and 4 mutants (Figure 2B). Furthermore, though the lower jaws form in a subset of *Snrpb*$^{ncc+/-}$ mutants, they were both asymmetrical and bilaterally smaller when compared to those of wild type embryos (Figure 2D, T-test, $p<.0001$). Additionally, the mandible showed incomplete fusion at the ventral end, and proximal structures such as the coronoid and the condylar processes, failed to form (Figure 2C). Additional defects included partial duplication of the proximal part of Meckel's cartilage, missing tympanic ring, hypoplasia or absence of the hyoid, and missing tracheal cartilages. Middle ear defects included partial duplication of the malleus and formation of ectopic cartilages, which could not be conclusively identified (n=4 of 7) (Figure 2E, SI 1D and SI 1F).

In addition to cartilage and skeletal abnormalities, the dorsal root ganglia, and cranial nerve ganglion – which form from ectodermal placodes and neural crest cells – were also abnormal in *Snrpb*$^{ncc+/-}$ mutants. Neurofilament staining of *Snrpb*$^{ncc+/-}$ mutant embryos showed that the cranial ganglia were reduced in size, and all had abnormal neuronal projection into the pharyngeal arches (n=2) (Figure 3A- 3D). The ophthalmic project of the trigeminal nerve (CN V) was reduced and did not extend over the lens, the maxillary projection appeared disorganized and missing, while the mandibular projection was reduced and appeared to have formed ventral

to the first arch. In addition, an ectopic projection was found in CN V in both mutants. Furthermore, the proximal portions of the geniculate (CN VII) and vestibulo-acoustic (CN VIII) ganglia were thicker than in control. Similarly, the glossopharyngeal nerve (CN IX) was abnormally thicker in the proximal region before the pharyngeal arch, had ectopic projection into pharyngeal arch 2, and reduced projection into pharyngeal arch 3. Finally, the proximal portion of the vagus nerve (CN X) was relatively normal but had an abnormal bundle at the distal end with reduced projections into the heart (Figure 3B). Furthermore, in addition to their reduced size, the dorsal root ganglia, of *Snrpb* heterozygous mutants also showed a bifurcation at the proximal end (Figure 3C, 3D).

Micro CT scans of E12.5, E14.5 and E17.5 embryos revealed a thinner cortex and enlarged lateral ventricles in $Snrpb^{ncc+/-}$ (Figure S5). In an E14.5, $Snrpb^{ncc+/-}$ embryo from group 4, the nasal septum and nasopharyngeal cavity were not formed, however, the oropharynx, tongue and pituitary gland were present (Figure S5A). At E17.5, a group 1 mutant embryo had missing nasal bones, unfused palatine shelves and cleft upper lips (Figure S5F). In addition, the aorticopulmonary septum which is derived from the cardiac neural crest cells failed to differentiate in this $Snrpb^{ncc+/-}$ embryo (Figure S5A-S5D), suggesting that cardiac neural crest cells failed to colonize and/or differentiate in the outflow tract. Furthermore, the thymus gland, a derivative of the third pharyngeal pouch, was not found in this mutant embryo (Figure S5E). Altogether, our morphological analysis indicates that *Snrpb* is required for the formation of structures that are derived from or induced by neural crests along the anterior-posterior axis. Our data also suggest that cardiac anomaly could contribute to the death of $Snrpb^{ncc+/-}$ embryos.

$Snrpb^{ncc+/-}$ mutants have increased cell death and reduced number of neural crest cells

To track $Snrpb^{ncc+/-}$ heterozygous neural crest cells and their derivatives we introduced the ROSA lacZ (Soriano P, 1999) and ROSA mT/mG (Mazumdar *et al.*, 2007) reporters into our mutant line. At E9.5, wild type and $Snrpb^{ncc+/-}$ mutant embryos (morphologically normal and abnormal) showed a comparable number of X-Gal positive mutant cells in the head and pharyngeal arches (Figure 3, SI 2) with no statistically significant difference (n=3) (SI 2C). However, at E10.5, morphologically abnormal mutant embryos (n=4) showed a reduced proportion of X-Gal positive cells in the developing head region (Figure 3 E-H), and this difference was statistically significant when compared to wild type (T-test, p=.003) (Figure 3I).

To determine if reduced proliferation and/or increased apoptosis contribute to loss of X-gal positive *Snrpb* heterozygous cells at E10.5, Phosphohistone H3 immunostaining and TUNEL assay, respectively, were performed. No significant changes in proliferation were found at E9.5 and E10.5 (SI 2J and SI 2K). However, a statically significant increase in TUNEL positive cells was found in the developing head region of E9.5 $Snrpb^{ncc+/-}$ embryos (T-test, p=.029) when compared to controls (Figure 3J- 3L). Our data indicate that *Snrpb* heterozygous cells migrate into the developing head region and the pharyngeal arches. However, a subset of these cells undergoes apoptosis and are lost in mutant embryos by E10.5.

Mutations in *Snrpb* causes an overall increase in both skipped exon (SE) and intron retention (IR)

To identify the molecular events that precede cell death in $Snrpb^{ncc+/-}$ embryos, head of E9.0 embryos with 11-13 somite pairs were isolated and used for RNA sequencing analysis. Surprisingly, gene expression data did not reveal a major distinction between mutant and control embryos and the samples did not cluster by genotype. This was further corroborated by differential gene expression (DEG) analysis, which identified very few (76) DEGs: 50 upregulated and 26 downregulated in the mutant embryos. This low number of DEGs is consistent with the lack of a clear phenotypic distinction at this developmental stage. However, the DEGs which were identified could already be characterized into relevant molecular pathways, specifically belonging to the p53 signaling pathway and representing components of the spliceosome (Figure 4A).

In contrast to the low number of DEGs, a large number of transcripts were found to be abnormally spliced. We identified 722 significant (FDR = 0.1) differentially spliced events (DSE) between the $Snrpb^{ncc+/-}$ (Het) and wildtype (WT) samples. The most abundant of these DSE were skipped exons (SE) and retained introns (RI) (Figure 4B). While the high proportion of SE could be expected based on prior alternative splicing studies, it was notable that more than 30% of the total AS events detected were RI events. We observed a strong tendency towards increased exon skipping and intron inclusion in the mutant samples; there were more SE (273 in Het versus 83 in WT) and RI (191 in Het versus 21 in WT) (Figure 4B). Consistent with the absence of significant gene expression changes, DSEs in $Snrpb^{ncc+/-}$ embryos did not lead to significant changes in inclusion of PTC containing exons or introns (Figure S6C and S6D).

However, SEs were more likely to be alternative exons (non-constitutive) in heterozygous (p=0.0034) versus wild type (Figure 4C and 4D), and expression of transcripts with splicing of constitutive exons was significantly reduced in mutants (p=0.0035) when compared to wild type (Figure 4E and 4F). Those global trends in splicing are consistent with those previously found in cell culture, suggesting that SNRPB deficiency results in increased skipping of alternatively spliced exons resulting from reduced recognition of splicing signals (Correa *et al.*, 2016).

We next investigated whether the aberrant splicing events in the mutant embryos could in fact be characterized by specific sequence features. We compared alternative events preferentially found in the mutants to two control groups: 1) events preferentially found in the wild-type embryos, and 2) a set of 1000 randomly chosen alternative events. Specifically, we aimed to test whether aberrant events in the mutants were associated with weaker splice signals. While there was a very slight trend towards weaker splice site scores (MaxEntScan, Yeo *et al.*, 2004) of RI in mutant embryos as compared to the controls, the differences were small and not statistically significant (Figure S6E and S6F). In contrast 5' SS strength was significantly higher in *Snrpb*$^{ncc+/-}$heterozygous embryos when compared to controls (Figure 4G,), while the 3' SS was comparable between mutants and controls (Figure 4H). We also analyzed the strength and position of predicted branch point (BP) signals (LaBranchoR, Paggi and Bejerano, 2018), but again we did not find notable differences (Figure S6K-S6N), with the exception of a slight preference for a more distal branch point location of mutant-specific SE events (27 bp in mutant versus 25 bp in the random set, p= 0.026). We also looked at general base composition in SE and RIs and no statistically significant difference was observed (Figure S6O-S6R), though the GC content in retained introns was slightly increased (Figure S6S and S6T). We also found no statistical differences in the length of SEs and RIs, although RIs were generally shorter in mutants when compared to wildtype (data not shown). Finally, we scanned for the frequency of RNA-binding protein motifs around the mutant specific events (rMAPS2, Jae Y Hwang *et al.* 2020), but did not identify significant enrichment of recognition signals of known splicing factors.

Overall, we did not find a compelling indication that the splicing aberrations present in mutants are linked to identifiable sequence features. The slight preference for stronger 5' SS, branch point site location (BPS) and intronic nucleotide composition are notable but will need

further scrutiny using more sensitive experimental designs. However, pathway analysis indicated that DSEs genes were significantly associated with mRNA processing (Figure 4K). Thus, the relatively large number of splicing aberrations, as compared to differentially expressed genes, detected at this developmental stage supports the hypothesis that these general splicing defects precede aberrations in gene expression and initiate the molecular cascade that leads to phenotypic changes. Thus, our next step was to conduct a thorough investigation of the lists of differentially spliced and expressed genes to identify the most likely candidates for triggering those events.

Increased skipping of *Mdm2* exon 3 and *Mdm4* exon 7, key regulators of P53, are associated with increase nuclear P53 in heads of *Snrpb*$^{ncc/+}$ embryos

We next investigated the key splicing changes that could explain craniofacial malformations in *Snrpb*$^{ncc+/-}$ embryos. We found increased skipping of exon 3 of *Mdm2* and exon 7 of *Mdm4*, regulators of the P53 pathway in our RNA-Seq analysis and confirmed these increases by RT-PCR (Figure 5). Increased skipping of these exons was previously reported in cultured *Snrpb* knockdown cells and shown to increase levels of nuclear P53 in mouse embryos with mutations in *Eftud2* a core component of the spliceosome (Beauchamp *et al.*, 2021, Alstyne *et al.*, 2018, Correa *et al.*, 2016). In fact, immunohistochemistry with an antibody to P53 revealed a significant enrichment of nuclear P53 in E9.5 mutant heads (Figure 5G and 5H). When expression of P53 and downstream genes were examined at E9.0, E9.5 and E11.5, we found no significant changes in *Trp53* levels (Figure 5I and 5J, Figure S7). In contrast, levels of the P53-pathway genes *Trp53inp1*, *Ccng1*, and *Phlda3* were significantly different from those of controls at E9.0 and E9.5 ($p=0.0352$, $p=0.0398$, $p=0.0459$, respectively, T-test) (Figure 5I and 5J) and not at E11.5 (Figure S7). Only *Ccng1* was significantly different between *Snrpb*$^{ncc+/-}$ and control embryos at E11.5 (Figure S7). Thus, we concluded that the increased exon skipping in *Mdm2* and *Mdm4* resulted in increased nuclear P53, and levels of P53 target genes in *Snrpb*$^{ncc+/-}$ embryos, prior to morphological abnormalities. Since P53 activation can lead to increased apoptosis, we postulate that increase P53 activity contributes to apoptosis of *Snrpb*$^{ncc+/-}$ mutant cells.

Reducing levels of P53 does not rescue craniofacial defects in *Snrpb*$^{ncc/+}$ embryos

We next tested if reducing levels of P53 prevent craniofacial malformations in *Snrpb*$^{ncc+/-}$ embryos. we crossed *Trp53*$^{loxp/+}$; *Wnt1-cre2*^{tg} mice and *Snrpb*$^{loxp/+}$ mice and collected E10.5 and E17.5 *Snrpb*$^{ncc+/-}$; *P53*$^{ncc+/-}$ double heterozygous embryos for analysis. At E17.5, when craniofacial defects were fully penetrant in *Snrpb*$^{ncc+/-}$ heterozygous mutants, no significant difference was found in the proportion of *Snrpb*$^{ncc+/}$*; P53*$^{ncc+/-}$ (n=4/4) embryos with craniofacial defects when compared to *Snrpb*$^{ncc+/-}$ mutants (n=3/3) (Figure S7B-S7E). We then generated *Snrpb*$^{ncc+/-}$ with two mutant *P53* alleles in their neural crest cells (*Snrpb*$^{ncc+/-}$; *P53*$^{ncc-/-}$) for cartilage analysis at E14.5. Though craniofacial defects were not severe in *Snrpb*$^{ncc+/-}$; *P53*$^{ncc-/-}$ mutant embryos, we did not recover any morphologically normal *Snrpb*$^{ncc+/-}$; *P53*$^{ncc-/-}$ mutant embryos (Figure S7F). Therefore, we propose that increased P53-mediated cell death alone was not responsible for craniofacial defects found in *Snrpb*$^{ncc+/-}$ mutant embryos.

Levels of core spliceosome transcripts are increased in *Snrpb*$^{ncc/+}$ heterozygous embryos.

We next examined expression of *Snrpb* and genes that form core components of the U2 and U5 snRNPs to determine if their levels are dysregulated in *Snrpb*$^{ncc+/-}$ heterozygous mutants. Expression of *Snrpb,* the U2 components, *Sf3b3* and *Sf3b4* and the U5 component *Eftud2* were analyzed from E9.0 – E11.5 by qRT-PCR. Levels of *Snrpb*, *Sf3b3, Sf3b4* and *Eftud2* were increased in E9.0 and E9.5 *Snrpb*$^{ncc+/-}$ embryos (Figure 6A, 6B, respectively). But these differences were only statistically significant between E9.5 controls and *Snrpb*$^{ncc+/-}$ embryos (p=0.0402, p=0.0340 and p=0.0352 respectively T-test) (Figure S6B). Since E8.5 heterozygous mutant embryos with deletion of the region that includes exons 2 and 3 of *Snrpb* have reduced expression of *Snrpb,* the increased expression of *Snrpb* found in *Snrpb*$^{ncc+/-}$ embryos are most likely due to neighboring wild type cells. Nonetheless, our data indicate that levels of core spliceosome genes are dysregulated in *Snrpb*$^{ncc/+}$ heterozygous mutants and that this may contribute to the significant difference in DSEs found in these mutants.

Genes important for craniofacial development are abnormally spliced in *Snrpb* $^{ncc+/-}$ mutants

To identify additional abnormal splicing events which could explain craniofacial malformations in *Snrpb* $^{ncc+/-}$ embryos, we queried the MGI database to determine if any transcripts with statistically significant DSEs were required for craniofacial development (Bogue

et al., 2017). We identified 13 transcripts required for craniofacial development or stem cell development with significant increases in exon skipping (See Table 1). Increased exon skipping in 5 of these genes: *Pdpk1, Rere (Atr2), Mcph1, Nf1,* and *Dyrk2*, is predicted to introduce a pretermination codon. RT-PCR analysis was used to examine presence of the predicted alternatively spliced products for *Smad2, Pou2f1* and *Rere* at E9.0, E9.5 and E11.5. This analysis revealed transcripts with the skipped exons were present in *Snrbp*$^{ncc+/-}$ mutant embryos at these stages. However, although the DSEs found in these transcripts were statistically significant in the RNAseq analysis, this was not the case by RT-PCR (Figure 6C-6H). These analyses showed that a number of genes important for craniofacial development are abnormally spliced in *Snrbp*$^{ncc+/-}$ embryos.

DISCUSSION

Splicing is an essential and ubiquitous process that generates mature mRNAs and increases the number and diversity of proteins in the human genome (Chen and Manley, 2009; Nilsen and Graveley, 2010). SNRPB is an essential protein that facilitates assembly of the snRNPs proteins that carry out splicing. Surprisingly, mutations that increase levels of a non-functional *SNRPB* transcript result in CCMS, a craniofacial spliceosomopathy that is also associated with rib defects (Lynch *et al.*, 2014). We successfully generated two mutant mouse lines, (Δ61 and *Snrpb*^{loxp}) and used them to interrogate the requirements for *Snrpb* during embryogenesis. We showed that *Snrpb* is haploinsufficient in mice and required for normal splicing of key regulators of P53 and transcripts required for normal craniofacial development. Our study show, for the first time, that levels of *Snrpb* and core spliceosomal genes that are regulated by it, are upregulated in the developing head when it is mutated in neural crest cells. Secondly, we show that morphological defects in *Snrpb* mutants were not associated with significant changes in gene expression but with alternative splicing suggesting that altered transcript ratios is responsible for defects and embryonic death of mutant embryos.

In patients with CCMS, increased level of a *SNRPB* transcript with a PTC containing alternative exon 2 is associated with defects mostly in the head and ribs (Lynch et al., 2014; Barcot et al., 2015 and Beauchamp et al., 2020). To examine the role of *SNRPB* in the development of tissues affected in patients, we first designed guide RNAs and repair templates to

generate a mutation in alternative exon 2 that would model those found in CCMS patients (data not shown). Although this strategy did not prove to be fruitful, we did recover a mutant mouse line with an intronic deletion of 61 base pairs near the alternative exon 2, when we tried to introduce loxP sequences into intron 2. Detailed morphological analysis of embryos and pups from this line revealed cartilage defects in the craniofacial region and ribs in association with an increase in the level of the PTC containing mouse *Snrpb* transcript indicating that in mouse, these structures are also more sensitive to levels of SNRPB. However, though the incomplete penetrance and variable expressivity found in the Δ61 mutant line is a classic CCMS feature (Tooley *et al.*, 2016), the reduced penetrance on three genetic backgrounds: CD1, FvB and C57Bl/6 (data not shown) makes this line intractable for molecular studies. Nonetheless, our findings revealed the existence of additional enhancer sequences in intron 2 of *Snrpb* that can regulate splicing of the PTC containing exon 2. This intronic region is conserved and should be interrogated in CCMS patients where a mutation was not identified by exome sequencing.

Although increased inclusion of the PTC containing alternative exon 2 leads to reduced levels of *Snrpb* (Lynch *et al.*, 2014), it was postulated that *SNRPB* mutations commonly found in CCMS patients are not loss of function mutations. We generated a conditional mutant allele which would lead to deletion of exon 2, alternative exon 2 and exon 3 in the presence of Cre. This deletion is predicted to generate a shorter *Snrpb* transcript of 527 bp (Figure S2B) that encodes for a non-functional protein. When β-*actin* cre was used to delete the loxp flanked exons throughout the embryo, heterozygous embryos died post-implantation. Therefore, we were unable to study the role of SNRPB in head and rib development in these $Snrpb^{+/-}$ mutants. Though further studies are needed to determine if there is a general growth defect or other roles for *Snrpb* at these early stages of development, our study indicates that heterozygosity for a loss of function allele of *Snrpb* is lethal. In fact, a single patient carrying a mutation in the 5' UTR of *SNRPB* that was predicted to result in a null allele was more severely affected and failed to survive gestation (Lynch *et al.*, 2014).

To study the role of SNRPB in craniofacial development we used the *Wnt1-Cre2* transgenic mouse line to generate embryos with heterozygous mutation of *Snrpb* in their neural tube and neural crest cells. In $Snrpb^{ncc+/-}$ mutant embryos, craniofacial structures derived from neural crest cells, such as the nasal bone, palates, maxilla, mandible, and middle ear structures, are abnormally formed. Intriguingly, these structures are also commonly reported to be affected

in CCMS patients, suggesting that abnormal neural crest cell survival and/or differentiation are responsible for defects in those patients. We also uncovered an absence or reduction of the hyoid bone (Figure 2) and ectopic cartilages and bones that we could not identify in some *Snrpb*$^{ncc+/-}$ mutants. Similarly, accessory ossicles in the hyoid bone were found after CT scan of two CCMS patients by Tooley *et al.*, 2016. We postulate that SNRPB is required in all neural crest cells, and their derivatives, a fact that is supported by the reduced or absent aorticopulmonary septum that is found in the microCT scan of *Snrpb*$^{ncc+/-}$ mutants. Furthermore, we propose that aorticopulmonary septal defects contribute to death of *Snrpb*$^{ncc+/-}$ embryos, as was found in *Eftud2*$^{ncc/+}$ mutants (Beauchamp *et al*., 2021). Finally, although phenotypes found in CCMS patients strongly suggested a requirement of SNRPB for endochondral ossification, our data clearly show abnormal development of bones formed via both endochondral and intramembranous ossification, indicating an early role for SNRPB in skeletal development.

In cell lines, knockdown of *SNRPB* decreased levels of the snRNAs that form the core of the U1, U4/U6, U5 and U6 snRNPs (Saltzman *et al.*, 2011). In addition, both splicing and/or expression of core genes of the U1, U2, U4/U6 and U5 snRNPs were dysregulated (Correa *et al.*, 2016). Thus, it was proposed that SNRPB plays a role in maintaining spliceosomal homeostasis. Our data also supports a role for SNRPB in spliceosomal homeostasis, as in *Snrpb*$^{ncc+/-}$ mutants, levels of *Snrpb* and of the U2 and U5 core splicing factors were increased. Additionally, as DSEs events identified in RNAseq analysis of the heads of *Snrpb*$^{ncc+/-}$ mutants were significantly associated with mRNA, our analyses provide strong evidence for a dysregulation in the splicing machinery in embryos with mutation in *Snrpb*, as was found in cells. Furthermore, since malformations in *Snrpb*$^{ncc+/-}$ mutants are mostly found in neural tube and neural crest derivatives, we postulate that the paradoxical increase in levels of splicing factors are in wildtype neighboring cells. However, future RNAseq experiments using sorted mutant cells or wild type neighboring cells are necessary to clarify which population show increases in splicing genes.

P53 stability and activity are known to be upregulated in response to mutation or disruption in the level of splicing factors (Alstyne *et al*., 2018, Correa *et al*. and 2016, Lei *et al*. 2020). In fact, we found increased skipping in two P53-regulators, *Mdm2* exon 3 and *Mdm4* exon 7, increased nuclear P53 and upregulation of P53 target genes in heads of E9.0 *Snrpb*$^{ncc+/-}$ mutants. In zebrafish and mouse, increased P53-activity contributes to craniofacial defects and knocking down or removing P53 genetically reduced apoptosis and improved development (Li

L. *et al*., 2017; Mao H. *et al*., 2016). Additionally, we showed that the P53-inhibitor, Pifithrin-α, improved head and brain development in embryos with mutation of *Eftud2* in the neural tube and neural crest (Beauchamp *et al*., 2021). However, reducing or removing P53 genetically in the neural crest cells did not show complete rescue of craniofacial defects in *Snrpb*$^{ncc+/-}$ mutant embryos. Although the variable expressivity found in *Snrpb*$^{ncc+/-}$ embryos, makes it difficult to rule out a partial rescue, our findings indicate that P53 alone is probably not responsible for the malformations we found.

Since RNAseq using the head of morphologically normal E9.0 *Snrpb*$^{ncc+/-}$ embryos revealed many more DSEs than DEGs and, pathway analysis revealed both DSE and DEGs were enriched in spliceosome and splicing, we propose that abnormal splicing underlies the defects found in mutant embryos. We confirmed differential splicing of the P53 regulators, *Mdm2* and *Mdm4* and identified 13 transcripts important for craniofacial development which were abnormally spliced in *Snrpb*$^{ncc+/-}$ embryos (Table 1). Though alternative splicing introduces a pretermination codon and is therefore predicted to perturb expression level in only 5 of these genes, alternative splicing can also modulate interaction and activity of proteins encoded by a gene. For example, increase skipping of exon 3 of *Smad2* makes a transcript which encodes for a protein that is a much more potent effector of TGFβ/Nodal than the full-length SMAD2. This shorter protein was shown to heterodimerizes with SMAD3 to regulate many developmental processes, including growth of the mandible (Dunn *et al*., 2005). Similarly, increased skipping of exon 8 of *Ror2* may disrupt the ability of this receptor to interact with *Wnt5* during midface, ear, and jaw development (Schwabe, G.C. *et al.*, 2004) Finally, though we did not find these splicing changes to be statistically significant by RT-PCR, the inclusion changes found for these exons are significant by RNAseq, a much more sensitive method for examining gene expression (Wang, Z. *et al.*, 2009)). Nonetheless, our RT-PCR analyses do confirm the existence of these transcripts, leading us to postulate that small increases in alternative splicing of these genes and others alters levels of transcripts required for morphogenesis and lead to an additive effect that culminates in malformations in *Snrbp* mutants.

Our working model is that dysregulation in the level of SNRPB, even if minor - as is likely the case with inclusion of the PTC containing alternative exon 2, perturbs the efficiency of splicing at the level of spliceosome assembly. It is likely that depending on the state of a given cell and the level of *Snrpb* in its neighbor, reduced levels of this gene will lead to a reduction or

an increase in core spliceosome genes. However, both reduced and increased levels of *Snrpb* are predicted to lead to malformations, as we found, suggesting that expression of this gene is tightly regulated. Furthermore, although cells with reduced levels of *Snrpb* have increased propensity to undergo apoptosis, we propose that splicing changes in important developmental genes, the proportion of cells that undergo apoptosis, and the timing of apoptosis all contribute to the variable expressivity found in *Snrpb* heterozygous mice and in CCMS patients. In conclusion, we believe that our work using the first CCMS animal model shows evidence for both ubiquitous and development specific roles of *Snrpb* during morphogenesis and provides much needed insights into the role of this splicing factor during embryogenesis.

ACKNOWLEDGEMENT

We would like to thank Dr. Mitra Cowan, Platform Manager, McGill Integrated Core of Animal Modeling (MICAM) for performing the microinjection experiments. This project was funded in parts by Canadian Institutes of Health Research (CIHR) and bridge funding from the Research Institute of McGill University Health Centre (RI-MUHC). We also thank Queen Elizabeth Scholars (QES) Program, Research Institute of McGill University Health Centre (RI-MUHC) and McGill Faculty of Medicine and Health Sciences for supporting Sabrina Alam. The funders had no role in study design, data collection and analyses, decision to publish or preparation of the manuscript. We acknowledge the professional and technical support from the Animal Resource Division (ARD) of RI-MUHC for maintaining our mice colonies. We are also thankful to the Small Animal Imaging Labs, Centre for Translational Biology, RI-MUHC for their support in performing the microCT scans. LJM and JM are members of the Research Centre of the McGill University Health Centre which is funded in parts by FRQS.

AUTHOR CONTRIBUTIONS

L.J.M. and J.M. conceptualized and supervised the project; E.B., R.P. and S.J.Z. analyzed all the RNA sequencing data, S.K. performed RT-qPCR experiments and analyses; M.C.B. and A.B. performed proliferation and apoptosis analysis and P53 immunohistochemistry; N.N. performed skeletal preparation analysis, S.S.A. performed all other experiments done in the study; L.J.M., J.M, and S.S.A wrote the manuscript with inputs from all authors.

DECLARATION OF INTERESTS

The authors declare no competing interests

FIGURE TABLE TITLES WITH LEGENDS

Figure 1: *Snrpb* heterozygosity is detrimental for mouse embryonic development. A. A representative *Snrpb*$^{del61/del61}$ embryo at E14.5 showing craniofacial abnormality with hypoplastic head and mandible, compared to the control littermate. B. Cartilage staining shows abnormal/absent craniofacial and rib cartilages in the face and ribs of a *Snrpb*$^{del61/del61}$ mutant at E14.5 (red arrows). C. *Snrpb*$^{ncc+/-}$ mutants at E14.5 and D. E17.5 show a range of abnormal craniofacial development, Group 2 had abnormal outer ear, cranial and mandibular hypoplasia, Group 3 had nasal clefts, Group 4 showed severe abnormalities including absence of the head and face. E=Ear, N=Nose, Fl=Forelimb, Hf=Headfold, Fb=Forebrain, Mb=Midbrain, Hb=Hindbrain, Ov=Otic vesicle, Ys=Yolk sac, Ht=Heart, Y=Eye, M=Mandible, 1=Pharyngeal arch 1, 2=Pharyngeal arch 2.

Figure 2: *Snrpb*$^{ncc+/-}$ embryos show abnormal craniofacial development. A. Sagittal and B. ventral view of E17.5 mutants showing abnormal formation of craniofacial bones. Neural crest cell derived bones (labeled in green letters) are predominantly affected in all *Snrpb*$^{ncc+/-}$ mutants. In B. ventral view of the skull showing palatal and maxillary clefts (star) in groups 2 and 3, respectively whereas in group 4 mutants did anterior craniofacial skeletal components do not form. C. Mandibles of mutants are abnormal, the condylar and coronoid processes are absent in mutants and left and right jaw were asymmetric. D. Both left and right mandibles are significantly shorter in *Snrpb*$^{ncc+/-}$ embryos ($p<.0001$, T-test), when compared to controls. E. Middle ear structures such as the stapes was absent in mutants, whereas duplicated Meckel's cartilage and ectopic structures were found in a subset of mutants. nc= nasal cartilage, nb=nasal bone, fb=frontal bone, ob=occipital bone, hb=hyoid bone, mn=mandible, pl=palatine, bo=basioccipital bone, bs=basisphenoid bone, cp=coronoid process, cn=condylar process, an=angle, mc=Meckel's cartilage, ml=melius, in=incus, st=stepes, sp=styloid process, PMX=premaxilla, MX=maxilla, PPMX= palatal process of maxilla, Za=zygomatic arch, As=alisphenoid bone, Sq=squamous bone

Figure 3: Increased cell death and abnormal neuronal development were evident in *Snrpb*$^{ncc+/-}$ mutants. A. 2H3 immunostaining showing normal cranial ganglia formation in a control embryo. B. *Snrpb*$^{ncc+/-}$ mutants (n=2) showed abnormal projections of nerves to the pharyngeal arches (cranial ganglion v and vii) and heart (cranial ganglion ix) and absence and bundle like structure formation of nerves (all are shown in black arrowheads). When compared to the controls in C., the dorsal root ganglia are bifurcated and reduced in mutants (arrowheads in D). E. and F. X-gal staining of E10.5 control and mutant embryos, respectively. F. shows fewer mutant cells in the craniofacial region and pharyngeal arches of the mutant (n=4) compared to the control embryo (n=4) in E. G, H, and I. Cryosection of an X-gal-stained embryos (n=3) showing a significant reduction in mutant cells when compared to control littermates (T-test, p<.005) J., K. and L show and increased (T-test, p<.05) TUNEL positive nuclei (red) found in *Snrpb*$^{ncc+/-}$ mutants (n=3) at E9.5 suggesting that an increase in cell death results in the reduction of mutant cells that are seen at E10.5. 1, 2, 3 =pharyngeal arches 1, 2 and 3, drg=dorsal root ganglia, fl=forelimb, hl=hindlimb, fb=forebrain, mb=midbrain, mx=maxillary prominence, hb=hindbrain, hm=head mesenchyme, nt=neural tube, ht=heart

Figure 4: *Snrpb*$^{ncc+/-}$ mutants show aberrant splicing that includes both increased exon skipping and intron retention. A. DEGs identified could grouped into molecular pathways belonging to the p53 signaling pathway and the spliceosome B. A much larger number of transcripts was found to be abnormally spliced in the *Snrpb*$^{ncc+/-}$ mutants. The most abundant of Differentially Spliced Exons (DSE) were skipped exons (SE) and retained introns (RI). A strong tendency towards increased exon skipping and intron inclusion in the mutant samples was observed; there were more SE (273 in Het versus 83 in WT) and RI (191 in Het versus 21 in WT). C.-F. Exon skipping was significantly higher for NonCE in the Het when constitutive (CE) vs Non-constitutive exons (Non-CE) were examined. G-J. For exon skipping, Splice site (SS) strength was significantly stronger 5'SS in mutants (P=.05). K. Pathway analysis of genes with DSEs showed that they were significantly associated with mRNA processing.

Figure 5: *Snrpb*$^{ncc+/-}$ mutants show increased exon skipping in two regulators of P53; *Mdm2* and *Mdm4*. A. and D. Sashimi plots of exon skipping events between *Snrpb*$^{ncc+/-}$ (Het, n = 3) and wild type (WT, n = 3) samples in *Mdm2* and *Mdm4*, respectively. The plots were rendered with sashimi with the genomic coordinates chr10:117688875-117710758 for *Mdm2* and

chr1:132986220-133025416 for *Mdm4*. Mutants showed an average of 1056 reads supporting the skipping of exon 2 and 3 in *Snrpb* while there were no alternative splicing events observed in WT. For *Mdm2*, there was an increased average number of reads supporting the skipping of exon 3 in Het compared to WT, from 27 reads in WT to 86 reads in Het. B. And E. RT-PCR showing full length and shorter transcripts with exons skipped in *Mdm2* and *Mdm4,* respectively in E9.0 control and mutant embryos. When quantified, a significant increase of the transcript with exon skipping was found in both C. *Mdm2* and F. *Mdm4* (t-test, $p<.05$). G. and H. Representative image showing increased nuclear P53 in an E9.5 mutant when compared to the control. I. and J. show significant changes in gene expression at E9.0 and E9.5, respectively, done by RT-qPCR. FL= full length transcript, ΔE3= transcript with exon 3 skipped, ΔE7= transcript with exon 7 skipped.

Figure 6: RT-PCR of E9.0 *Snrpb*$^{ncc+/-}$ mutants to validate exon skipping in genes important for craniofacial development. A. and B. Show mRNA expression of U2 and U5 core components at E9.0 and E9.5, respectively, by RT-qPCR. C, D and E. shows sashimi plot for the exon skipping events found for *Smad2, Pou2f1* and *Rere*. On the right of each gene's sashimi plot, representative gel for RT-PCR show verification of the exon skipping event. The bottom of each gel shows the location of the primers used to amplify the transcripts. In *Smad2,* exon 3 is skipped (C), exon 4 *Pou2f1* (D), whereas exon 4 is skipped in *Rere* (E). F., G., and H. Quantification of splicing (skipped exon transcript / full-length transcript) did not show any significant differences in exon skipping between control and mutant samples (T-test). FL=Full length, ΔE=skipped exon.

TABLE WITH TITLE AND LEGEND

Gene name	Skipped Exon	PTC	Phenotype	Constitutive exon
1. Smad2	Exon 3	No	Mandible hypoplasia (Nomura and Li, 1998)	No
2. Loxl3	Exon 2	No	Cleft palate, short and bent mandible (Zhang *et al.*, 2015)	No
3. Ror2	Exon 8	No	Midface hypoplasia, truncated Meckel's, middle ear defect (Schwabe, G.C. *et al.*, 2004)	Yes

4. Nisch	Exon 6	No	Short snout (Crompton, M. *et al.*, 2017)	Yes
5. Pou2f1	Exon 4	No	Abnormal nasal placode development when removed with *Sox2* (Donner, A.L. *et al.*, 2006)	Yes
6. Rgl1	Exon 3	No	Abnormal frontal bone, short snout, abnormal maxilla and mandibular morphology (Mouse Genome Informatics and the International Mouse Phenotyping Consortium, 2014)	Yes
7. Frem1	Exon 32	No	Midface hypoplasia, asymmetry, short snout (Vissers, L.E. *et al.*, 2011)	Yes
8. Smc3	Exon 5	No	Upturned snout (White, J.K. *et al.*, 2013)	Yes
9. Pdpk1	Exon 3	Yes	Abnormalities in the head, nasal cartilage (Lawlor, M.A. *et al.*, 2002)	Yes
10. Rere (*Atr2*)	Exon 4	Yes	Small pharyngeal arch (Zoltewicz, J.S. *et al.*, 2004)	Yes
11. Mcph1	Exon 13	Yes	Microcephaly (Gruber, R. *et al.*, 2011)	Yes
12. Nf1	Exon 56	Yes	Head hyperplasia, aorticopulmonary septal defect, heart defects (Brannan, C.I. *et al.*, 1994)	Yes
13. Dyrk2	Exon 2	Yes	Cleft palate (Yoshida, S. *et al.*, 2020)	No

Table 1: Increased SE of craniofacial developmental genes in *Snrpb* $^{ncc+/-}$ mutants Transcripts required for normal head/craniofacial development with a significant increase in skipped exons are not all predicted to result in PTC in *Snrpb*$^{ncc+/-}$.

STAR METHODS

Resource Availability

Lead contact

Further information and requests for resources and reagents should be directed to and will be fulfilled by the Lead Contact, Loydie A. Jerome-Majewska (loydie.majewska@mcgill.ca).

Materials Availability

All antibodies, chemicals and most mouse lines used in this study are commercially available. All other unique materials are available upon request.

Data and code availability

Accession IDs provided by GEO: GSE180546, GSM5464627, GSM5464628, GSM5464629, GSM5464630, GSM5464631, GSM5464632

METHOD DETAILS

Mouse lines

All procedures and experiments were performed according to the guidelines of the Canadian Council on Animal Care and approved by the animal Care Committee of the Montreal Children's Hospital. Wild type CD1, mT/mG *Gt(ROSA)26Sor*$^{tm4(ACTB\text{-}tdTomato,\text{-}EGFP)Luo}$*/J* , (Soriano, 1999)**.** *Wnt1-Cre2, β-actin-cre* mice were purchased. The *R26R* strain (Gt (ROSA)26Sor^{tm1Sor} (Mazumdar et al., 2007) was a kind gift from Dr. Nagano.

Generation and establishment of *Snrpb* Δ61 and conditional mutant mouse lines

To develop a conditional knock-out *Snrpb* allele, we used CRISPR/Cas9-mediated homology-directed repair (HDR) strategy to insert LoxP sequences flanking exon-2. Probable efficient guide RNAs were selected based on previous references (Xu et. al., 2015). All the microinjections were performed by Dr. Mitra Cowan at McGill Integrated Core of Animal Modeling (MICAM). Microinjection with single-strand DNA template, guide RNAs, and Cas9 mRNA was done. Initially, Intron 1 and intron 2 were targeted with the guide sequences to insert LoxP sequences. The 61 bp intronic deletion allele was recovered from microinjection experiments targeting exon 2. In the subsequent microinjections, intron 3 was targeted to flank the region containing exons 2 and 3 of *Snrpb* with Loxp sequences, to not interrupt intron 2. In the first round of microinjection targeting intron 1, a Loxp sequence was inserted in intron 1 of 25% of the animals born. The insertion was confirmed in two animals (1 male and 1 female) by Sanger sequencing. We generated homozygous animals with Loxp sequences in intron 1 from

these animals and they were used for the second round of microinjection to insert Loxp in intron 3. Sanger sequencing of DNA from a G1 male offspring of a targeted founder from the second round of microinjection and a wild type CD1 female was used to confirm that both Loxp sequences in intron 1 and intron 3 were intact. Thereafter, we backcrossed the animals for at least 5 generations to establish the *Snrpb* conditional mutant mouse line and to remove any potential off-target effect from CRISPR editing.

Generation of *Snrpb* $^{+/-}$ mutant embryos

To generate constitutive *Snrpb* $^{+/-}$ mutants, beta actin-Cre $^{tg/+}$ mice were mated with Snrpb$^{loxp/+}$ mice. From these matings, dissections were done from E6.5 – E10.5 to collect *Snrpb* $^{loxp/+}$*; Wnt1-Cre* $^{tg/+-}$ heterozygous embryos.

Generation neural crest cell-specific *Snrpb* $^{+/-}$ mutants

To generate embryos and animals with neural crest specific *Snrpb* knockout, *Wnt1-Cre2* $^{tg/+}$ animals were mated with *Snrpb* $^{loxp/+}$ mice. Embryos obtained from these matings were *Snrpb* heterozygous mutant in the neural crest cells and their derivatives, while all other cells were *Snrpb* wild type.

Genotyping of mice and embryos

Genomic DNA was extracted from mouse tails or yolk sacs by alkaline lysis (Hou, Gupta *et al*., 2017). For *Snrpb,* genotyping was performed to identify the wildtype and conditional allele (with LoxP sequences) to amplify segments of intron 1 using the following program: 30 sec 95°C, 30 sec 62°C, 30 sec 72°C for 35 cycles followed by an elongation step of 10 minutes at 72°C. This PCR amplified the targeted DNA segment to determine a wild-type (347 bp) and a mutant (387 bp) amplicon. The primers used for the genotyping were: forward-CCCGAGACAGACACAACATAAG, reverse-GCTTTGAAGGTCCCGATGAA. For the commercially available lines, namely R26R, *Wnt1-Cre2*, mT/mG and beta-actin cre genotyping was performed as detailed on Jackson`s laboratory website: protocol# 29915 (*R26R*), #25394 (*Wnt1-Cre2*), #20368 (mT/mG) and ##33618 (beta-actin cre), respectively.

Collection of embryos

Male and female were put together overnight, females were checked for vaginal plugs on the morning of the next day and were considered embryonic day 0.5 (E0.5), if plugged. Embryos were collected at specific days of development and yolk sacs were used for genomic DNA extraction genotyping. During dissection, the number of somites of each embryo was counted under the microscope for stages E8.5 to E10.5. Live embryos were determined based on the presence of heart-beat. Embryos were examined for phenotypic abnormalities and any resorption was noted. Embryos were then fixed in 4% paraformaldehyde in PBS at 4°C overnight (unless otherwise stated), washed and kept in PBS at 4°C until later use.

Preparation of embryos for embedding

Dissected embryos were fixed in 4% paraformaldehyde overnight and dehydrated using a graded methanol series for wholemounts. Wholemount *in situs* were performed as previously described (Revil and Jerome-Majewska 2013). For cryo-embedding, fixed embryos were first cryoprotected in 30% sucrose overnight and sectioned at 10mm thickness for IF and IHC.

Cartilage staining of embryos

To investigate cartilage formation, embryos were stained with Alcian Blue (Regeur, 2013). Freshly dissected E14.5 embryos were fixed in Bouin's fixing solution for 2 hours followed by several washes in ammonium hydroxide and ethanol solution, until they were completely white. Embryos were then washed in acetic acid and stained in an Alcian blue staining solution (0.03% Alcian blue in 80% ethanol; 20% acetic acid) for 24-48h at 37°C. BABB (benzyl alcohol: benzyl benzoate, 1:2) solution was used to clear the embryos and analysed under the light microscope.

Skeletal Preparation of embryos and pups

Briefly, for skeletal staining, the skin was removed from freshly dissected E17.5 embryos and neonatal pups. The viscera were removed carefully and the embryos/pups were fixed in 100% ethanol for 24 hours, transferred to acetone and then stained with staining solution (1 volume 0.3% Alcian Blue, 1 volume 0.1% Alizarin Red, 1 volume Glacial Acetic Acid, 17 volumes 70%

ethanol) for 3-4 days at 37°C. The tissues were mostly cleared by 1% potassium hydroxide for 3-4 days at room temperature and the rest of the remaining tissues were cleared up using a series of glycerol solutions in 1% KOH. Finally, skeletons were preserved at 50% glycerol in 1% KOH. Skeletal preparations were analysed and imaged.

Wholemount X-galactosidase staining of embryos

After fixing embryos at 4% paraformaldehyde in PBS for about an hour, they were washed in a detergent rinse solution (0.02% Igepal, 0.01% sodium deoxycholate, 2mM $MgCl_2$ in 0.1M phosphate buffer pH 7.5) 3 times for 15 minutes each. They were then stained with freshly prepared 1mg/ml X-gal staining solution (0.02% Igepal, 0.01% Sodium Deoxycholate, 5mM Potassium Ferricyanide, 5mM Potassium Ferrocyanide, and 2mM $MgCl_2$ in 0.1M phosphate buffer pH 7.5) overnight at 37°C in the dark. After washing with PBS, the stained embryos were post-fixed overnight in 4% paraformaldehyde in PBS at 4°C. Embryos were then embedded in Cryomatrix and stored at -80°C until sectioning. After sectioning, slides were washed 2 times in PBS for 5 mines each and then nuclear fast red counterstained for 5 mins. Slides were then mounted with aqueous mounting media and pictures were taken. Image J was used to quantify the lacz stained area.

PTA staining for CT scan

Embryos were fixed overnight in 4% PFA and then washed with PBS. After a series of dehydration according to the protocol describe previously (Lesciotto et al., 2020) embryos were stained in 0.7% Phosphotungstic Acid (PTA). The duration of staining varied depending on the stage of the embryos and pre-scanning were done to confirm complete penetration of the PTA into the embryos. Once all the structures were visualised in the pre-scan, embryos were rehydrated in a series of methanol and CT scanning was done at 20-micrometer thickness.

Immunofluorescence and TUNEL assay

Immunofluorescence experiments were performed according to standard protocols (Zakariyah et al., 2011). The following primary antibodies were used: Phosphohistone H3 (Ser10) (1:200

dilution). Alexa Fluor 568 (1:500 dilutions) secondary antibody was used. For the quantification of apoptosis, TUNNEL assay was performed according to the manufacturer`s protocol for the cell death detection kit. Slides were mounted with VECTASHIELD hard-set mounting medium with DAPI to visualize the nuclei and images were captured with a fluorescence microscope. For quantification of fluorescence signal, particle analysis on Image J was used.

Immunohistochemistry

P53 primary antibody was used (1:250 dilution) and the VECTASTAIN® Universal Quick HRP Kit was used as secondary antibody and visualized with DAB. After rinsing with water, slides were mounted with an aqueous mounting medium and images were captured.

Western Blotting

Heads of E10.5 embryos of CD1 genetic background were lysed in RIPA buffer (25 mM Tris·HCl pH 7.6, 10% glycerol, 420 mM NaCl, 2 mM $MgCl_2$, 0.5% NP-40, 0.5% Triton X-100, 1 mM EDTA, protease inhibitor) on ice. Embryos were sonicated and centrifuged at 13000rpm for 20 minutes at 4°C. Protein lysates were measured according to standard methods using a DC protein assay kit. 50μg of protein was resolved on 12% SDS gels and then transferred to PVDF membranes. Membranes were blocked in 5% milk and were probed with primary antibody (SNRPB 1:1000). Visualization of the protein was done using horseradish peroxidase-conjugated secondary antibody and antigen-antibody complexes were detected using the ECL system. Images of western blots were taken with Bio-Rad's ChemiDoc MP System and were digitally analyzed using Image Lab software. To normalize the level of protein of interest, beta-actin was used as a control.

RNA isolation for RNA sequencing

RNA extraction was done using Qiagen RNeasy kit following manufacturer's protocol from samples stored in RNA later (Invitrogen). For RNA isolation at E9.0, heads of two somite-

matched embryos from different litters were pooled according to genotype. 3 wild type and heterozygous pools were used for RNA sequencing analysis.

qRT-PCR

Total RNA was treated with DNAse (NEB, according to manufacturer's protocol) and used for reverse transcription with the iScript™ Reverse Transcription Supermix for RT. qRT-PCR was performed using the ssoAdvanced universal SYBR® Green Supermix. RT-qPCR experiments were performed in duplicates to ensure technical replicability. Target genes were normalized with the normalization factor as calculated by geNorm software (Vandesompele et a. 2002). Three house-keeping genes including B2M, GAPDH, and SDHA were used for generation of the normalization factor as previously reported (Vandesompele et a. 2002).

RNA sequencing Analysis

Sequencing libraries were prepared by McGill Genome Centre (Montreal, Canada), using the TruSeq Stranded Total RNA Sample Preparation Kit (Illumina TS-122-2301, San Diego, California, United States) by depleting ribosomal and fragmented RNA, synthesizing first and second strand cDNA, adenylating the 3′ ends and ligating adaptors, and enriching the adaptor-containing cDNA strands by PCR. The libraries were sequenced using the Illumina NovaSeq 6000 PE100 sequencer, 100 nucleotide paired-end reads, generating between 109 and 230 million reads sample. The sequencing reads were trimmed using CutAdapt (Martin M., 2011)and mapped to the mouse reference genome (mm10) using STAR (Dobin A et al., 2013) aligner (version 2.6.1d), with default parameters, and annotated using the Gencode (Harrow J *et al.*, 2006) M2 (version M2, 2013) annotation. htseq-count (part of the 'HTSeq' (Anders S *et al.*, 2015) framework, version 0.13. 5) was used for expression quantification.

To perform a differential splicing analysis, rMATS 4.0.2 (Shen S. *et al.*, 2014) was used and detected splicing events were filtered by systematically excluding those with a mean of inclusion junction counts (IJC) lower than 5 in either wild-type or heterozygous samples. To identify significant DSE, an absolute inclusion level difference (ILD) cut-off of more than 0.05

was used and a Benjamin-Hochberg multiple testing correction with a False Discovery Rate (FDR) cut-off of less than 0.1 was used. The rationale for relaxing the FDR cut-off here was to obtain a large dataset enriched for alternative splicing events in order to observe general tendencies, such as increased propensity for exon skipping or intron retention in the mutants. To characterize 3'SS sequences, LaBranchoR (Paggi and Bejerano, 2018), a branchpoint (BP) prediction tool based on a deep-learning approach was used, that uses a bidirectional long short-term memory network (LSTM) model, to identify relevant branchpoints upstream DSEs. The BPs and their surrounding area consensus motifs were generated using WebLogo 3.0 (Crooks GE *et al.*,2004).

For differential expression analysis (DEA), we used DESeq2 (Love M.I. e*t al.*, 2014) package and a list of significant DEG was derived using a FDR cut-off of less than 0.05 with no additional restriction on the absolute log2 fold change (Log2FC) (to allow for detection of even minor expression changes). For KEGG pathway analyses, the combined list of up- and down-regulated genes from DEA was used as input to gProfiler2 (Raudvere U. et al., 2019) package (gost function), and all the detected genes from DEA were used as background.

A differential analysis of transposable element (TE) and lncRNA expression was also carried out, to investigate whether SNRPB deficiency may result in deregulation of the non-coding transcriptome. Those analyses did not uncover any differences in the mutant embryos, and the results are not shown in the manuscript. STAR was used to map the processed reads with modified options:—outFilterMultimapNmax 100 —winAnchorMultimapNmax 100 —outMultimapperOrder Random —alignSJoverhangMin 8 —outFilterMismatchNmax 999 —alignIntronMin 20 —alignIntronMax 1000000 —alignMatesGapMax 1000000, with mouse annotations to guide mapping, coming from the UCSC repeat masker (Gencode M1) and lncRNA (Gencode M1) annotations. The mapped lncRNA and TE reads were respectively quantified with salmon (Patro R. *et al.*, 2017) and TElocal (Jin Y *et al.*, 2014). Differential lncRNA and TE expression analysis were performed using DESeq2, with the TE and lncRNA read counts being normalized using protein-coding gene expression size factors and differentially expressed lncRNA and TE selected based on a FDR cut-off of less than 0.05 and an absolute Log2FC of greater than 0.5 to increase detection signal.

Quantification and Statistical analysis

Quantitation was performed using Image J software (NIH). Statistical analyses were conducted using GraphPad Prism 8.0 software (GraphPad Prism, San Diego, CA, USA). Two-tailed unpaired Man Whitney t-test analysis was calculated Prism Software and Chi-square test was also calculated using Prism. Significant p-values are represented as *P<0.05, **P<0.01 and ***P<0.001.

SUPPLEMENTARY INFORMATION TITLES AND LEGENDS

Figure S1, related to figure 1: A 61 base pair intronic deletion in *Snrpb* causes developmental abnormalities in mice. A. An allele with a 61bp intronic deletion near the alternative exon 2 in *Snrpb* was generated by *CRISPR Cas9* editing. B. When compared to the control (left), both heterozygous and homozygous P0 pups with the del61 mutation showed abnormal craniofacial development. C., D., and E. A subset of *Snrpb* del61 mutants shows abnormal limb development such as polydactyly (in D) and clinodactyly (in E, arrowhead). F. Skeletal staining of a *Snrpb* del61 heterozygous mutant showing extra pair of rib development (arrowhead). G. Bar graph showing percentages of different abnormalities found in *Snrpb* del61 mutants. H. A significant portion of the mutants die over different times. Each drop in the line denotes death of an animal. I. RT-PCR showing inclusion of AE2 in *Snrpb* del61 mutants (blue arrow), and the protein -coding transcript (purple arrow). J. and K. Western blot revealed a subset of *Snrpb* del61 heterozygous and homozygous mutants produced lower levels of SNRPB than the control embryos. E=Ear, N=Nose, Hl=Hindlimb

Figure S2, related to figure 1: *Snrpb* heterozygosity causes embryonic lethality before morphogenesis A. Generation of $Snrpb^{+/-}$ allele by mating *Snrpb* loxp mice with *Beta-actin* cre mice. B. $Snrpb^{+/-}$ mutant embryos produce a shorter transcript of 527 base-pairs (primers amplified exon 1 to exon 6). C. RT-qPCR analysis revealed a significant decrease in *Snrpb* level in E8.5 heterozygous mutant embryos.

Figure S3, related to figure 1 and figure 2 : $Snrpb^{ncc+/-}$ mutants are found at P0. A. Generation of $Snrpb^{ncc+/-}$ allele by mating *Snrpb* loxp mice with *Wnt-1 Cre2* transgenic mice. B.

Control P0 pup (n=3) showing normal craniofacial development whereas in C. *Snrpb*$^{ncc+/-}$ mutant pups have an abnormally shaped head, micrognathia and abnormal outer ears. D *Snrpb*$^{ncc+/-}$ mutant pups lack milk spot in their stomach (black arrowhead), which is visible in the control littermate (white arrowhead). E. and F. Higher magnification showing a hypoplastic pinna in the *Snrpb*$^{ncc+/-}$ mutant (black arrow). G. Skeletal staining revealed palatal cleft in mutants (yellow arrowhead), and abnormal alisphenoid and basisphenoid bones in ventral views. H. Mandibles of *Snrpb*$^{ncc+/-}$ mutants are abnormal. Arrow indicate abnormal structures in mutant mandibles. I. The lateral view of mutants. The tympanic ring is absent or very hypoplastic and ectopic bone formation was seen (white arrowhead in the mutant) E=ear, Y= eye, Fl=forelimb, Tb=temporal bone, Bs=basisphenoid bone, As= Alisphenoid bone, PL=palatine, PMX=premaxilla, PPPMX= palatal process of premaxilla, PPMX= palatal process of maxilla, Tr=tympanic ring of ear, AP=angular process, CP=coronoid process, CNP=condyloid process, MC=meckel's cartilage. Triangles represent loxp sequences, rectangles represent exons

Figure S4, related to figure 1 and figure 2: *Snrpb*$^{ncc+/-}$ embryos show craniofacial abnormalities from E9.5 onward. A. At E9.0 (13 somites), mutant embryos could not be distinguished from control littermates. B. At E9.5 50% of *Snrpb*$^{ncc+/-}$ embryos had hypoplastic forebrain, midbrain and hindbrain. C. By E10.5, 70% of the *Snrpb*$^{ncc+/-}$ embryos were abnormal with smaller pharyngeal arches and abnormal forebrain and midbrain. D. E11.5 *Snrpb*$^{ncc+/-}$ mutants were grouped into three where group one was normal, and group 2 had hypoplasia of the forebrain, midbrain and hindbrain as wells as reduced maxillary and mandibular prominences. Group 3 mutants did not form the maxillary and mandibular prominences. E. At E12.5, 4 groups were found, group1 was normal, group 2 mutants had clefts in the face, group3 had abnormal forebrain with complete facial cleft and group 4 mutants did not develop any forebrain and anterior facial structures at all. F. Similar craniofacial abnormalities were also found at E14.5 and G. onward at E17.5, except group1. E=eye, N=nose, Y=Ear, fl=forelimb, hl=hindlimb, fb=forebrain, mb=midbrain, hb=hindbrain, 1, 2= pharyngeal arch 1 and 2, respectively.

Figure S5, related to figure 1 and figure 2: Micro CT scan of *Snrpb*$^{ncc+/-}$ mutants show abnormal development of heart, brain, palate and thymus. A. MicroCT scan revealed a thinner cortex and larger lateral ventricle in the E14.5 mutant, when compared to the littermate

control. The nasopharyngeal cavity and nasal septum were absent in the mutant. Scan of control E17.5 embryo (n=1). Panel C. shows a close up of the heart (in B.) from posterior to anterior (left to right of the panel), and formation of the aorticopulmonary septum (white arrowhead) separating the aorta and pulmonary arteries in the control. E. In an E17.5 *Snrpb*$^{ncc+/-}$ mutant the aorticopulmonary septum was missing (red arrowhead). F. Sagittal view of a *Snrpb*$^{ncc+/-}$ mutant showing the absence of the thymus (red arrowhead) which can be seen in the control embryo (white arrowhead). F. Palatal shelves, which are fused (white arrowheads) in the control embryo, did not fuse in the *Snrpb*$^{ncc+/-}$ mutant. A cleft in the maxilla is also shown in the mutant (yellow arrowhead) LV=left ventricle, RV=Right ventricle, Tg=Tongue, Th=Thymus, Nc=Nasopharyngeal cavity, lv=lateral ventricle, Op=Oropharynx, Ao=Aorta, Pa=Pulmonary artery, Pg=Pituitary gland, Bs=basisiphenoid bone, Ps=Palatal shelve, Mx=Maxilla

Figure S6, related to figure 4: Specific sequence features analyses that might contribute to aberrant splicing in the *Snrpb*$^{ncc+/-}$ mutants. Effects of Premature termination codons (PTCs) in exons that are more skipped in the mutant (A) and wild-type embryos (B) on the exon Inclusion Level. No significant difference was observed between (more skipped) PTC and Non-PTC exons. Similarly, C**.** and D**.** show effects of PTCs in the exons that are more skipped in the mutant (C) and wild-type embryos (D) on the expression of genes carrying those exons. No significant difference was observed in expression of genes with (more skipped) PTC and Non-PTC exons. E. and F. Splice site weakness assessment (MaxEntScan scores): comparative analysis of the 5 'splice site strength (E) and 3’ splice site strength (F) of introns that are more retained in mutant embryos and wild-type embryos, respectively. No significant difference was found in both analyses between the 2 conditions (Significance cut-offs, p-value <= 0.1[*] or p-value <= 0.05[**]). G and H. A 9-mer (3 exonic flanks and 6 intronic flanks around the 5'ss) consensus motif derived from introns that are more retained in mutant embryos (G) and wild-type embryos (H). I and J. A 23-mer (20 intronic flanks and 3 exonic flanks around the 3'ss) consensus motif derived from introns that are more retained in mutant embryos (I) and wild-type embryos (J). K. highlights a significant difference in the strength of the BP sites (taking into account the LaBranchoR BP scores, 23bp upstream the 3’SS of exons that are more skipped in mutant embryos in comparison of those skipped in the wild-type embryos). L. A mean comparison test (t-test) of the BP Distance from the 3’SS of the exons that are more skipped in mutant compared to the wild-type embryos. M. highlights a mean comparison test (t-test) of the

LaBranchoR predicted BP Score from the introns that are more retained in mutant embryos in comparison to those more retained in the wild-type embryos, with no significant difference. N. A mean comparison test (t-test) of the BP Distance from the 3'SS of the introns that are more retained in the mutant compared to the wild-type embryos. - Significance cutoffs used: p-value > 0.05 [ns] and p-value <= 0.05[*]. O and P. A (consensus) motif analysis of the branchpoint site (23bp around the LaBranchoR predicted branchpoint [BP]) from exons that are more skipped in mutant embryos (O) and wild-type embryos (P). Q and R. A (consensus) motif analysis of the branchpoint sites (23bp around the LaBranchoR predicted BPS) from introns that are more retained in mutant (Q) and wild-type embryos (R). S and T. show a GC content analysis (G+C nucleotide frequency analysis) of the 23bp sequences, upstream the LaBranchoR predicted BP of exons that are more skipped (S) and more retained (T) in mutant and wild-type embryos. A clear higher GC proportion in the mutant embryos is seen in case of retained intron.

Figure S7, related to figure 5: Knockdown of P53 in the neural crest cells do not rescue the craniofacial abnormalities in *Snrpb*$^{ncc+/-}$ mutants. RT-PCR of E11.5 *Snrpb*$^{ncc+/-}$ mutant heads revealed a significant increase (T-test) in *Ccng1*. B. E10.5 *Snrpb*$^{ncc+/-}$ embryos (n=4) with heterozygous knockdown of P53 in the neural crest cells are phenotypically similar to *Snrpb*$^{ncc+/-}$ embryos. C. Similar range of phenotypic abnormalities was found in E17.5 *Snrpb*$^{ncc+/-}$ embryos heterozygous for P53 when compared to *Snrpb*$^{ncc+/-}$ embryos (shown in Figure 1) D. Skeletal staining of E17.5 *Snrpb*$^{ncc+/-}$;*P53*$^{ncc+/-}$ embryos (Figure 2A), showing that P53 heterozygosity in neural crest cells do not rescue craniofacial abnormalities in *Snrpb*$^{ncc+/-}$ embryos . E. At E14.5 *Snrpb*$^{ncc+/-}$;*P53*$^{ncc-/-}$ embryos showed milder abnormalities in the middle ear and Meckel's cartilage. Nt=neural tube, hm=head mesenchyme. E=Ear, M=Mandible, fl=forelimb, hb=hindbrain, mb=midbrain, fb=forebrain, mc=Meckel's cartilage.

SI 1, related to figure 2, figure S4: E14.5 *Snrpb*$^{ncc+/-}$ mutants show abnormal cartilage development in the head and face. A. Sagittal view of embryos showing a group 2 mutant with a shorter and discontinuous Meckel's cartilage(mc) (red arrowhead), group 3 mutant with reduced head cartilage and Meckel's cartilage (red arrowhead), and a group 4 mutant with no anterior craniofacial cartilages, when compared to normal wildtype littermate (white arrowhead).

B. ventral view of the head shows cartilage developmental abnormalities as described for panel A. D. and F. Ectopic cartilages shown in red arrowhead were also seen in a subset of the *Snrpb*$^{+/-}$ mutants (n=4/7), while compared to controls (C. and E.) mc=Meckel's cartilage, nc=nasal cartilage.

SI 2, related to figure 3: Neural crest cells migrate to the pharyngeal arches of E9.5 *Snrpb*$^{ncc+/-}$ mutants and show no significance difference in their numbers when compared to control embryos. A. Representative image of X-gal stained E9.5 *Snrpb*$^{ncc+/-}$ embryos (n=3) showing mutant cells (in blue) in the craniofacial region and pharyngeal arches. B. and C. Cryosection and quantification of blue cells revealed a non-significant reduction in the percentage of mutant cells in *Snrpb*$^{ncc+/-}$ embryos when compared to controls. D. and F. Lower magnification image of *Snrpb* control and mutant embryos, respectively, carrying the mT/mG reporter. Embryos were stained with DAPI and green fluorescent marks *Wnt1* cre-expressing cells. F. and G. show higher magnification of the craniofacial region of the same control and mutant embryos, respectively, where presence of mutant cells was found in the mutant embryos similar as the panel A mutant. H. and I. A magnified view of the pharyngeal arch of cryosectioned embryos (n=3) showing presence of mutant cells (green) in the pharyngeal arches of mutants and controls (in H). J and K. Phosphohistone staining (Black) at E9.5 and E10.5, respectively, on x-gal stained embryo sections. Quantification revealed no significant difference between controls and mutants at both stages. hb=hindbrain, mb=midbrain, fb=forebrain, pa=pharyngeal arch, nt=neural tube, ncc=neural crest cells, mc=mesenchymal core, 1,2=pharyngeal arch 1 and 2, respectively

SI 3, related to figure S4: Mendelian segregation table for neural Crest cell specific *Snrpb* mutant embryos. Dead embryos found at: E9.5, n=11, At E12.5, n=1, At E14.5, n=5, At E17.5, n=4, *** =** Chi-Square test is significant ($p<.05$). Dead embryos were excluded from the Chi-square test at all stages. Resorptions are not typed

SI 4, related to figure S3: Mendelian segregation table for neural Crest cell specific *Snrpb* mutant animals. At P0, 5 mutants were recovered from 6 litters. However, at P1 and P21 no mutants were found

References:

1. Anders, S., Pyl, P.T., and Huber, W. (2015). HTSeq--a Python framework to work with high-throughput sequencing data. Bioinformatics 31, 166-169. 10.1093/bioinformatics/btu638.
2. Bacrot, S., Doyard, M., Huber, C., Alibeu, O., Feldhahn, N., Lehalle, D., Lacombe, D., Marlin, S., Nitschke, P., Petit, F., et al. (2015). Mutations in SNRPB, encoding components of the core splicing machinery, cause cerebro-costo-mandibular syndrome. Hum Mutat 36, 187-190. 10.1002/humu.22729.
3. Beauchamp, M.C., Alam, S.S., Kumar, S., and Jerome-Majewska, L.A. (2020). Spliceosomopathies and neurocristopathies: Two sides of the same coin? Dev Dyn 249, 924-945. 10.1002/dvdy.183.
4. Beauchamp, M.C., Djedid, A., Bareke, E., Merkuri, F., Aber, R., Tam, A.S., Lines, M.A., Boycott, K.M., Stirling, P.C., Fish, J.L., et al. (2021). Mutation in Eftud2 causes craniofacial defects in mice via mis-splicing of Mdm2 and increased P53. Hum Mol Genet 30, 739-757. 10.1093/hmg/ddab051.
5. Bogue, M.A., Grubb, S.C., Walton, D.O., Philip, V.M., Kolishovski, G., Stearns, T., Dunn, M.H., Skelly, D.A., Kadakkuzha, B., TeHennepe, G., et al. (2017). Mouse Phenome Database: an integrative database and analysis suite for curated empirical phenotype data from laboratory mice. Nucleic Acids Research 46, D843-D850. 10.1093/nar/gkx1082.
6. Brannan, C.I., Perkins, A.S., Vogel, K.S., Ratner, N., Nordlund, M.L., Reid, S.W., Buchberg, A.M., Jenkins, N.A., Parada, L.F., and Copeland, N.G. (1994). Targeted disruption of the neurofibromatosis type-1 gene leads to developmental abnormalities in heart and various neural crest-derived tissues. Genes Dev 8, 1019-1029. 10.1101/gad.8.9.1019.

7. Chen, M., and Manley, J.L. (2009). Mechanisms of alternative splicing regulation: insights from molecular and genomics approaches. Nat Rev Mol Cell Biol 10, 741-754. 10.1038/nrm2777.
8. Correa, B.R., de Araujo, P.R., Qiao, M., Burns, S.C., Chen, C., Schlegel, R., Agarwal, S., Galante, P.A., and Penalva, L.O. (2016). Functional genomics analyses of RNA-binding proteins reveal the splicing regulator SNRPB as an oncogenic candidate in glioblastoma. Genome Biol 17, 125. 10.1186/s13059-016-0990-4.
9. Crompton, M., Purnell, T., Tyrer, H.E., Parker, A., Ball, G., Hardisty-Hughes, R.E., Gale, R., Williams, D., Dean, C.H., Simon, M.M., et al. (2017). A mutation in Nischarin causes otitis media via LIMK1 and NF-kappaB pathways. PLoS Genet 13, e1006969. 10.1371/journal.pgen.1006969.
10. Crooks, G.E., Hon, G., Chandonia, J.M., and Brenner, S.E. (2004). WebLogo: a sequence logo generator. Genome Res 14, 1188-1190. 10.1101/gr.849004.
11. Dobin, A., Davis, C.A., Schlesinger, F., Drenkow, J., Zaleski, C., Jha, S., Batut, P., Chaisson, M., and Gingeras, T.R. (2013). STAR: ultrafast universal RNA-seq aligner. Bioinformatics 29, 15-21. 10.1093/bioinformatics/bts635.
12. Donner, A.L., Episkopou, V., and Maas, R.L. (2007). Sox2 and Pou2f1 interact to control lens and olfactory placode development. Dev Biol 303, 784-799. 10.1016/j.ydbio.2006.10.047.
13. Dunn, N.R., Koonce, C.H., Anderson, D.C., Islam, A., Bikoff, E.K., and Robertson, E.J. (2005). Mice exclusively expressing the short isoform of Smad2 develop normally and are viable and fertile. Genes Dev 19, 152-163. 10.1101/gad.1243205.
14. Fregeau, B., Kim, B.J., Hernandez-Garcia, A., Jordan, V.K., Cho, M.T., Schnur, R.E., Monaghan, K.G., Juusola, J., Rosenfeld, J.A., Bhoj, E., et al. (2016). De Novo Mutations of RERE Cause a Genetic Syndrome with Features that Overlap Those Associated with Proximal 1p36 Deletions. Am J Hum Genet 98, 963-970. 10.1016/j.ajhg.2016.03.002.
15. Gruber, R., Zhou, Z., Sukchev, M., Joerss, T., Frappart, P.O., and Wang, Z.Q. (2011). MCPH1 regulates the neuroprogenitor division mode by coupling the centrosomal cycle with mitotic entry through the Chk1-Cdc25 pathway. Nat Cell Biol 13, 1325-1334. 10.1038/ncb2342.

16. Harrow, J., Denoeud, F., Frankish, A., Reymond, A., Chen, C.K., Chrast, J., Lagarde, J., Gilbert, J.G., Storey, R., Swarbreck, D., et al. (2006). GENCODE: producing a reference annotation for ENCODE. Genome Biol 7 Suppl 1, S4 1-9. 10.1186/gb-2006-7-s1-s4.
17. Hou, W., Gupta, S., Beauchamp, M.C., Yuan, L., and Jerome-Majewska, L.A. (2017). Non-alcoholic fatty liver disease in mice with heterozygous mutation in TMED2. PLoS One 12, e0182995. 10.1371/journal.pone.0182995.
18. Hwang, J.Y., Jung, S., Kook, T.L., Rouchka, E.C., Bok, J., and Park, J.W. (2020). rMAPS2: an update of the RNA map analysis and plotting server for alternative splicing regulation. Nucleic Acids Res 48, W300-W306. 10.1093/nar/gkaa237.
19. Jin, Y., Tam, O.H., Paniagua, E., and Hammell, M. (2015). TEtranscripts: a package for including transposable elements in differential expression analysis of RNA-seq datasets. Bioinformatics 31, 3593-3599. 10.1093/bioinformatics/btv422.
20. Jones, N.C., Lynn, M.L., Gaudenz, K., Sakai, D., Aoto, K., Rey, J.P., Glynn, E.F., Ellington, L., Du, C., Dixon, J., et al. (2008). Prevention of the neurocristopathy Treacher Collins syndrome through inhibition of p53 function. Nat Med 14, 125-133. 10.1038/nm1725.
21. Lawlor, M.A., Mora, A., Ashby, P.R., Williams, M.R., Murray-Tait, V., Malone, L., Prescott, A.R., Lucocq, J.M., and Alessi, D.R. (2002). Essential role of PDK1 in regulating cell size and development in mice. EMBO J 21, 3728-3738. 10.1093/emboj/cdf387.
22. Lei, L., Yan, S.Y., Yang, R., Chen, J.Y., Li, Y., Bu, Y., Chang, N., Zhou, Q., Zhu, X., Li, C.Y., and Xiong, J.W. (2017). Spliceosomal protein eftud2 mutation leads to p53-dependent apoptosis in zebrafish neural progenitors. Nucleic Acids Res 45, 3422-3436. 10.1093/nar/gkw1043.
23. Lesciotto, K.M., Motch Perrine, S.M., Kawasaki, M., Stecko, T., Ryan, T.M., Kawasaki, K., and Richtsmeier, J.T. (2020). Phosphotungstic acid-enhanced microCT: Optimized protocols for embryonic and early postnatal mice. Dev Dyn 249, 573-585. 10.1002/dvdy.136.
24. Lewis, A.E., Vasudevan, H.N., O'Neill, A.K., Soriano, P., and Bush, J.O. (2013). The widely used Wnt1-Cre transgene causes developmental phenotypes by ectopic activation of Wnt signaling. Dev Biol 379, 229-234. 10.1016/j.ydbio.2013.04.026.

25. Love, M.I., Huber, W., and Anders, S. (2014). Moderated estimation of fold change and dispersion for RNA-seq data with DESeq2. Genome Biol 15, 550. 10.1186/s13059-014-0550-8.
26. Lynch, D.C., Revil, T., Schwartzentruber, J., Bhoj, E.J., Innes, A.M., Lamont, R.E., Lemire, E.G., Chodirker, B.N., Taylor, J.P., Zackai, E.H., et al. (2014). Disrupted auto-regulation of the spliceosomal gene SNRPB causes cerebro-costo-mandibular syndrome. Nat Commun 5, 4483. 10.1038/ncomms5483.
27. Mao, H., McMahon, J.J., Tsai, Y.H., Wang, Z., and Silver, D.L. (2016). Haploinsufficiency for Core Exon Junction Complex Components Disrupts Embryonic Neurogenesis and Causes p53-Mediated Microcephaly. PLoS Genet 12, e1006282. 10.1371/journal.pgen.1006282.
28. Muzumdar, M.D., Tasic, B., Miyamichi, K., Li, L., and Luo, L. (2007). A global double-fluorescent Cre reporter mouse. Genesis 45, 593-605. 10.1002/dvg.20335.
29. Nilsen, T.W., and Graveley, B.R. (2010). Expansion of the eukaryotic proteome by alternative splicing. Nature 463, 457-463. 10.1038/nature08909.
30. Nomura, M., and Li, E. (1998). Smad2 role in mesoderm formation, left-right patterning and craniofacial development. Nature 393, 786-790. 10.1038/31693.
31. Olthof, A.M., Hyatt, K.C., and Kanadia, R.N. (2019). Minor intron splicing revisited: identification of new minor intron-containing genes and tissue-dependent retention and alternative splicing of minor introns. BMC Genomics 20, 686. 10.1186/s12864-019-6046-x.
32. Paggi, J.M., and Bejerano, G. (2018). A sequence-based, deep learning model accurately predicts RNA splicing branchpoints. RNA 24, 1647-1658. 10.1261/rna.066290.118.
33. Patro, R., Duggal, G., Love, M.I., Irizarry, R.A., and Kingsford, C. (2017). Salmon provides fast and bias-aware quantification of transcript expression. Nat Methods 14, 417-419. 10.1038/nmeth.4197.
34. Raudvere, U., Kolberg, L., Kuzmin, I., Arak, T., Adler, P., Peterson, H., and Vilo, J. (2019). g:Profiler: a web server for functional enrichment analysis and conversions of gene lists (2019 update). Nucleic Acids Res 47, W191-W198. 10.1093/nar/gkz369.

35. Revil, T., and Jerome-Majewska, L.A. (2013). During embryogenesis, esrp1 expression is restricted to a subset of epithelial cells and is associated with splicing of a number of developmentally important genes. Dev Dyn 242, 281-290. 10.1002/dvdy.23918.
36. Saltzman, A.L., Pan, Q., and Blencowe, B.J. (2011). Regulation of alternative splicing by the core spliceosomal machinery. Genes Dev 25, 373-384. 10.1101/gad.2004811.
37. Schwabe, G.C., Trepczik, B., Suring, K., Brieske, N., Tucker, A.S., Sharpe, P.T., Minami, Y., and Mundlos, S. (2004). Ror2 knockout mouse as a model for the developmental pathology of autosomal recessive Robinow syndrome. Dev Dyn 229, 400-410. 10.1002/dvdy.10466.
38. Scotti, M., and Kmita, M. (2012). Recruitment of 5' Hoxa genes in the allantois is essential for proper extra-embryonic function in placental mammals. Development 139, 731-739. 10.1242/dev.075408.
39. Shen, S., Park, J.W., Lu, Z.X., Lin, L., Henry, M.D., Wu, Y.N., Zhou, Q., and Xing, Y. (2014). rMATS: robust and flexible detection of differential alternative splicing from replicate RNA-Seq data. Proc Natl Acad Sci U S A 111, E5593-5601. 10.1073/pnas.1419161111.
40. Soriano, P. (1999). Generalized lacZ expression with the ROSA26 Cre reporter strain. Nat Genet 21, 70-71. 10.1038/5007.
41. Tooley, M., Lynch, D., Bernier, F., Parboosingh, J., Bhoj, E., Zackai, E., Calder, A., Itasaki, N., Wakeling, E., Scott, R., et al. (2016). Cerebro-costo-mandibular syndrome: Clinical, radiological, and genetic findings. Am J Med Genet A 170A, 1115-1126. 10.1002/ajmg.a.37587.
42. Van Alstyne, M., Simon, C.M., Sardi, S.P., Shihabuddin, L.S., Mentis, G.Z., and Pellizzoni, L. (2018). Dysregulation of Mdm2 and Mdm4 alternative splicing underlies motor neuron death in spinal muscular atrophy. Genes Dev 32, 1045-1059. 10.1101/gad.316059.118.
43. Vandesompele, J., De Preter, K., Pattyn, F., Poppe, B., Van Roy, N., De Paepe, A., and Speleman, F. (2002). Accurate normalization of real-time quantitative RT-PCR data by geometric averaging of multiple internal control genes. Genome Biol 3, RESEARCH0034. 10.1186/gb-2002-3-7-research0034.

44. Vissers, L.E., Cox, T.C., Maga, A.M., Short, K.M., Wiradjaja, F., Janssen, I.M., Jehee, F., Bertola, D., Liu, J., Yagnik, G., et al. (2011). Heterozygous mutations of FREM1 are associated with an increased risk of isolated metopic craniosynostosis in humans and mice. PLoS Genet 7, e1002278. 10.1371/journal.pgen.1002278.
45. Wang, Z., Gerstein, M., & Snyder, M. (2009). RNA-Seq: a revolutionary tool for transcriptomics. Nature reviews. Genetics, 10(1), 57–63. https://doi.org/10.1038/nrg2484
46. White, J.K., Gerdin, A.K., Karp, N.A., Ryder, E., Buljan, M., Bussell, J.N., Salisbury, J., Clare, S., Ingham, N.J., Podrini, C., et al. (2013). Genome-wide generation and systematic phenotyping of knockout mice reveals new roles for many genes. Cell 154, 452-464. 10.1016/j.cell.2013.06.022.
47. Wickramasinghe, V.O., Gonzalez-Porta, M., Perera, D., Bartolozzi, A.R., Sibley, C.R., Hallegger, M., Ule, J., Marioni, J.C., and Venkitaraman, A.R. (2015). Regulation of constitutive and alternative mRNA splicing across the human transcriptome by PRPF8 is determined by 5' splice site strength. Genome Biol 16, 201. 10.1186/s13059-015-0749-3.
48. Xu, H., Xiao, T., Chen, C.H., Li, W., Meyer, C.A., Wu, Q., Wu, D., Cong, L., Zhang, F., Liu, J.S., et al. (2015). Sequence determinants of improved CRISPR sgRNA design. Genome Res 25, 1147-1157. 10.1101/gr.191452.115.
49. Yeo, G., and Burge, C.B. (2004). Maximum entropy modeling of short sequence motifs with applications to RNA splicing signals. J Comput Biol 11, 377-394. 10.1089/1066527041410418.
50. Yoshida, S., Aoki, K., Fujiwara, K., Nakakura, T., Kawamura, A., Yamada, K., Ono, M., Yogosawa, S., and Yoshida, K. (2020). The novel ciliogenesis regulator DYRK2 governs Hedgehog signaling during mouse embryogenesis. Elife 9. 10.7554/eLife.57381.
51. Zakariyah, A., Hou, W., Slim, R., and Jerome-Majewska, L. (2012). TMED2/p24beta1 is expressed in all gestational stages of human placentas and in choriocarcinoma cell lines. Placenta 33, 214-219. 10.1016/j.placenta.2011.12.009.
52. Zhang, J., Yang, R., Liu, Z., Hou, C., Zong, W., Zhang, A., Sun, X., and Gao, J. (2015). Loss of lysyl oxidase-like 3 causes cleft palate and spinal deformity in mice. Hum Mol Genet 24, 6174-6185. 10.1093/hmg/ddv333.

53. Zhu, L., Zhang, X., and Sun, Z. (2020). SNRPB promotes cervical cancer progression through repressing p53 expression. Biomed Pharmacother 125, 109948. 10.1016/j.biopha.2020.109948.
54. Zoltewicz, J.S., Stewart, N.J., Leung, R., and Peterson, A.S. (2004). Atrophin 2 recruits histone deacetylase and is required for the function of multiple signaling centers during mouse embryogenesis. Development 131, 3-14. 10.1242/dev.00908.

FIGURE 1

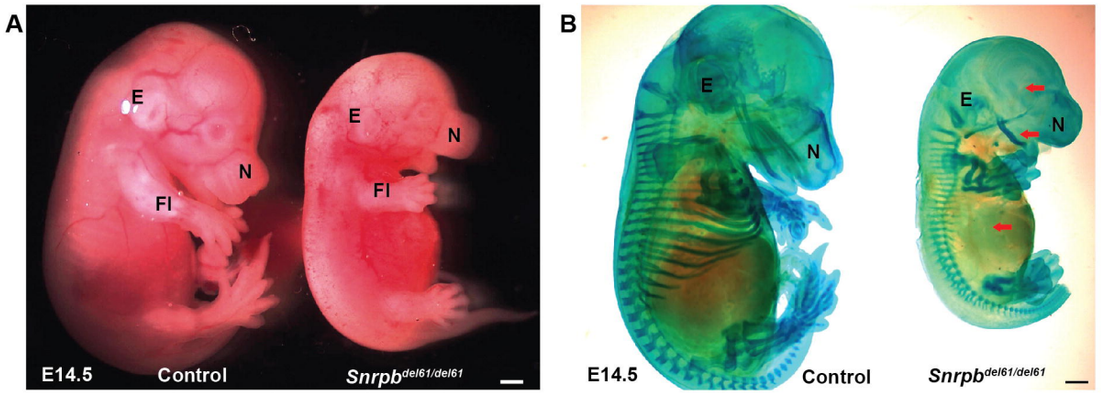
A
E
N
Fl
E
N
Fl
E14.5
Control
Snrpb del61/del61
B
E
N
E
N
E14.5
Control
Snrpb del61/del61

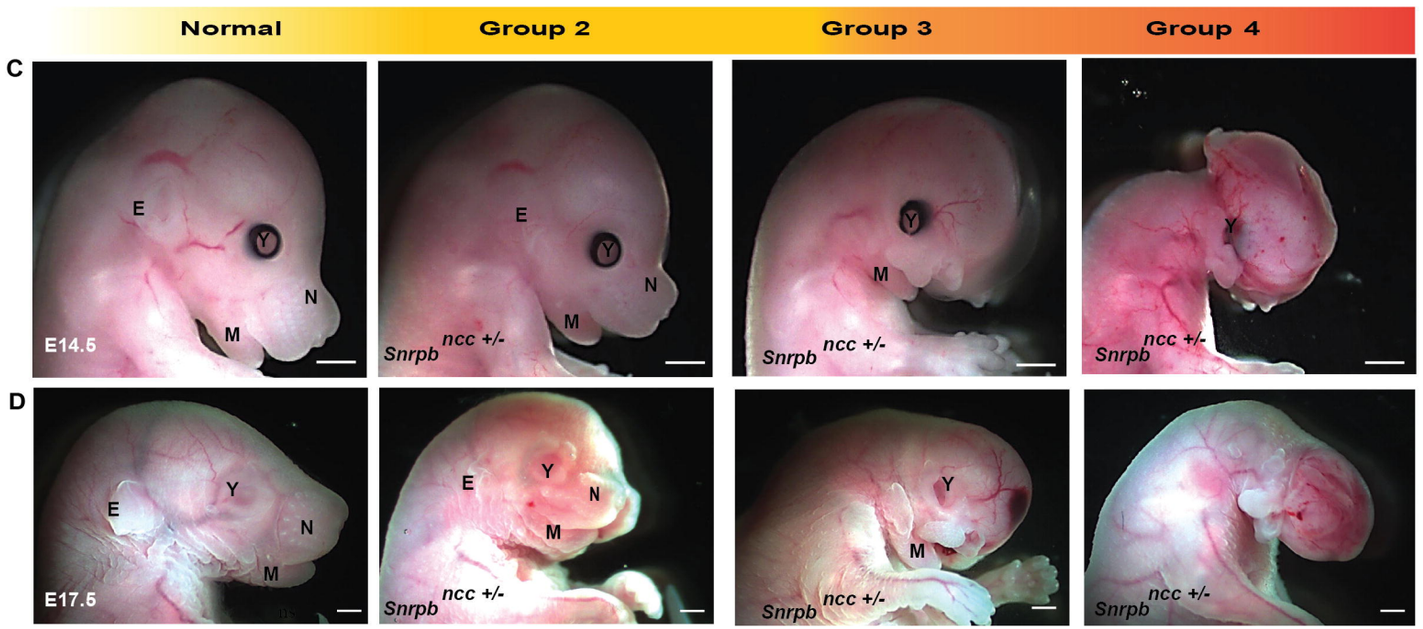
Normal
Group 2
Group 3
Group 4
C
E
Y
N
M
E14.5
Snrpb ncc +/-
D
E17.5

FIGURE 2

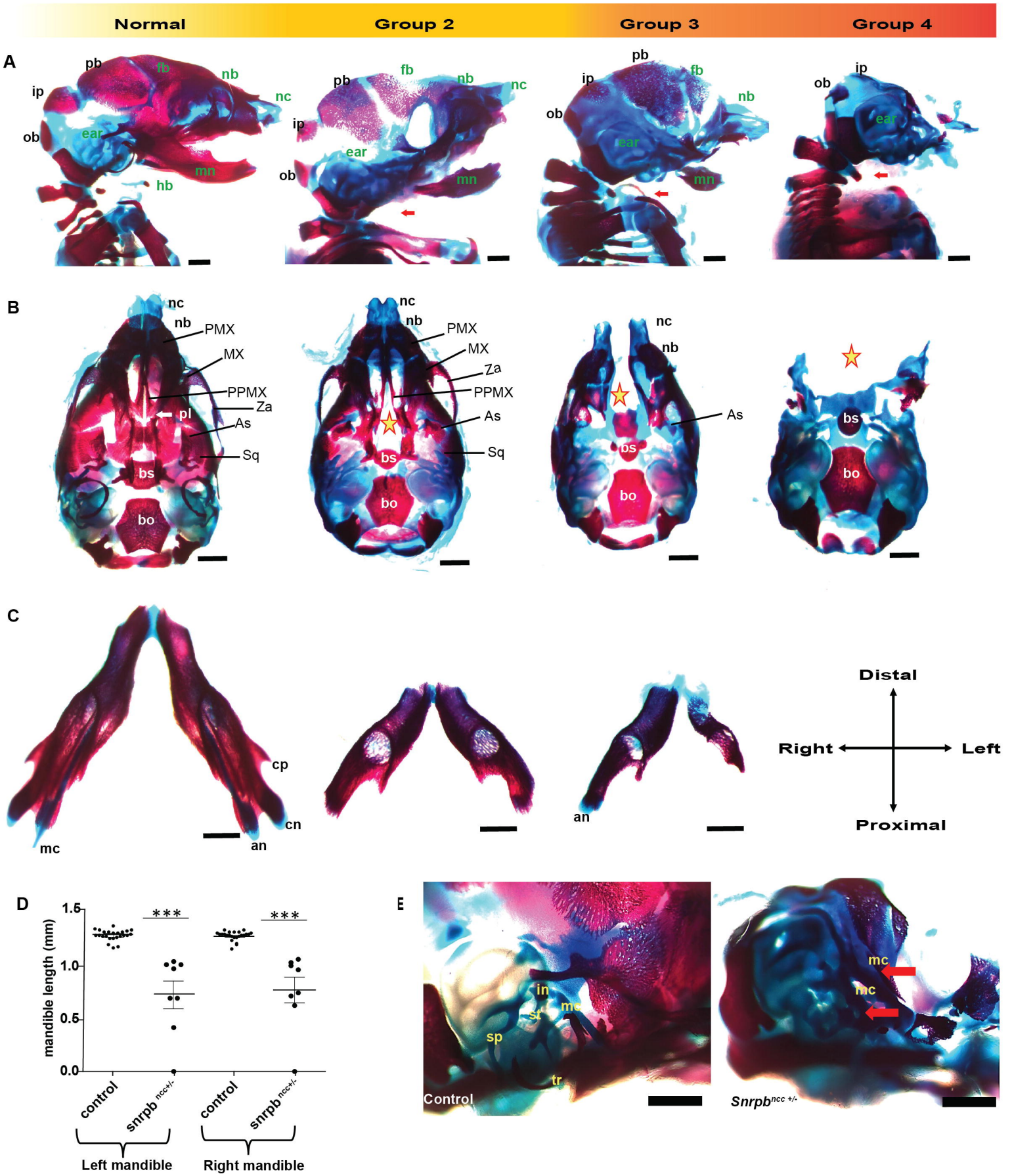
Normal
Group 2
Group 3
Group 4
A
pb
fb
nb
nc
ip
ob
ear
mn
hb
B
PMX
MX
PPMX
Za
pl
As
Sq
bs
bo
C
cp
cn
mc
an
Distal
Proximal
Right
Left
D
mandible length (mm)
1.5
1.0
0.5
0.0
***
control
snrpb ncc+/-
Left mandible
Right mandible
E
in
st
me
sp
tr
Control
mc
Snrpb ncc +/-

FIGURE 3

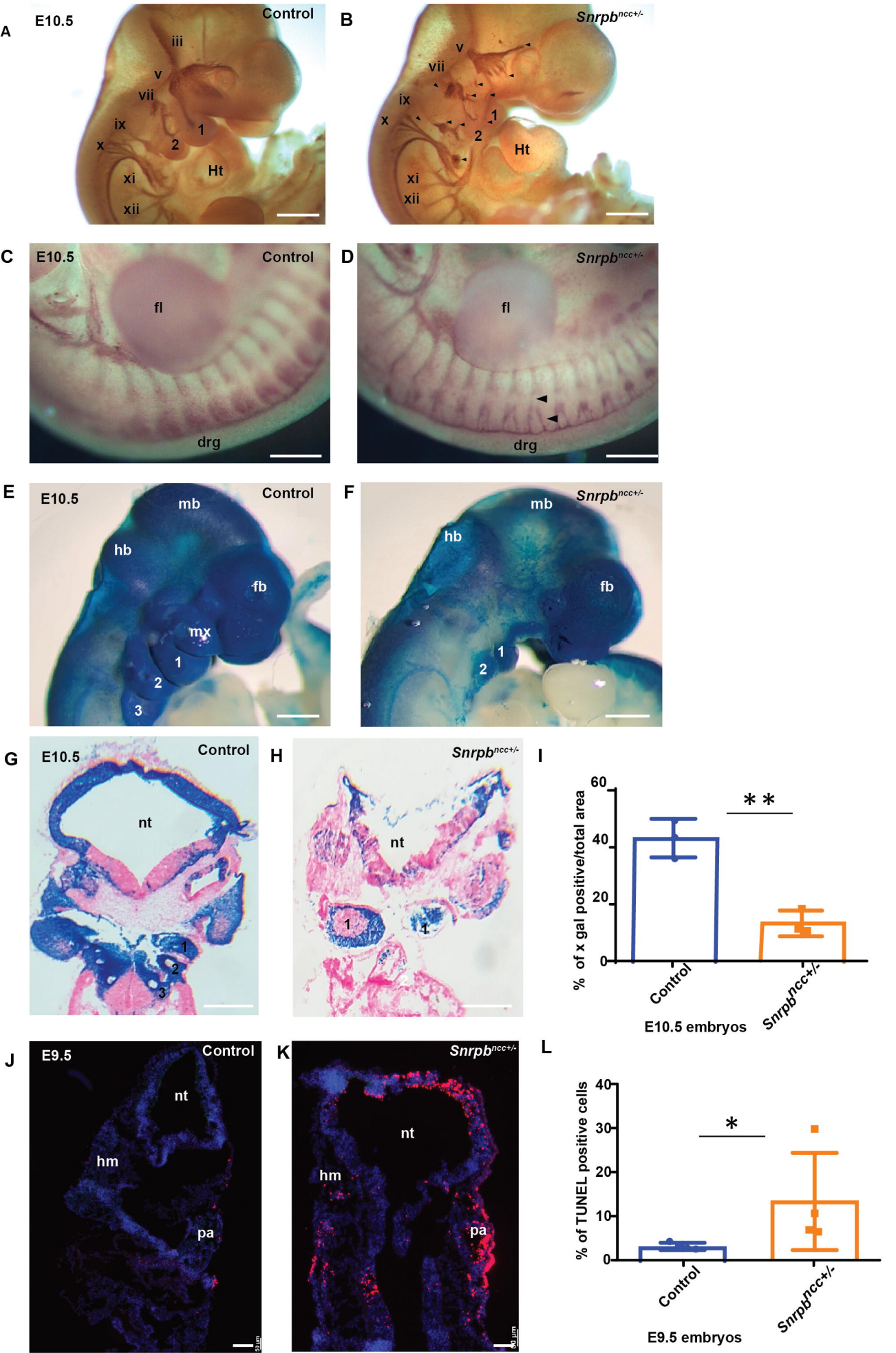
A
E10.5
Control
iii
v
vii
ix
x
1
2
Ht
xi
xii
B
Snrpb ncc+/-
v
vii
ix
x
1
2
Ht
xi
xii
C
E10.5
Control
fl
drg
D
Snrpb ncc+/-
fl
drg
E
E10.5
Control
mb
hb
fb
mx
1
2
3
F
Snrpb ncc+/-
mb
hb
fb
1
2
G
E10.5
Control
nt
1
2
3
H
Snrpb ncc+/-
nt
1
1
I
60
40
20
0
% of x gal positive/total area
**
Control
Snrpb ncc+/-
E10.5 embryos
J
E9.5
Control
nt
hm
pa
K
Snrpb ncc+/-
nt
hm
pa
L
40
30
20
10
0
% of TUNEL positive cells
*
Control
Snrpb ncc+/-
E9.5 embryos

FIGURE 4

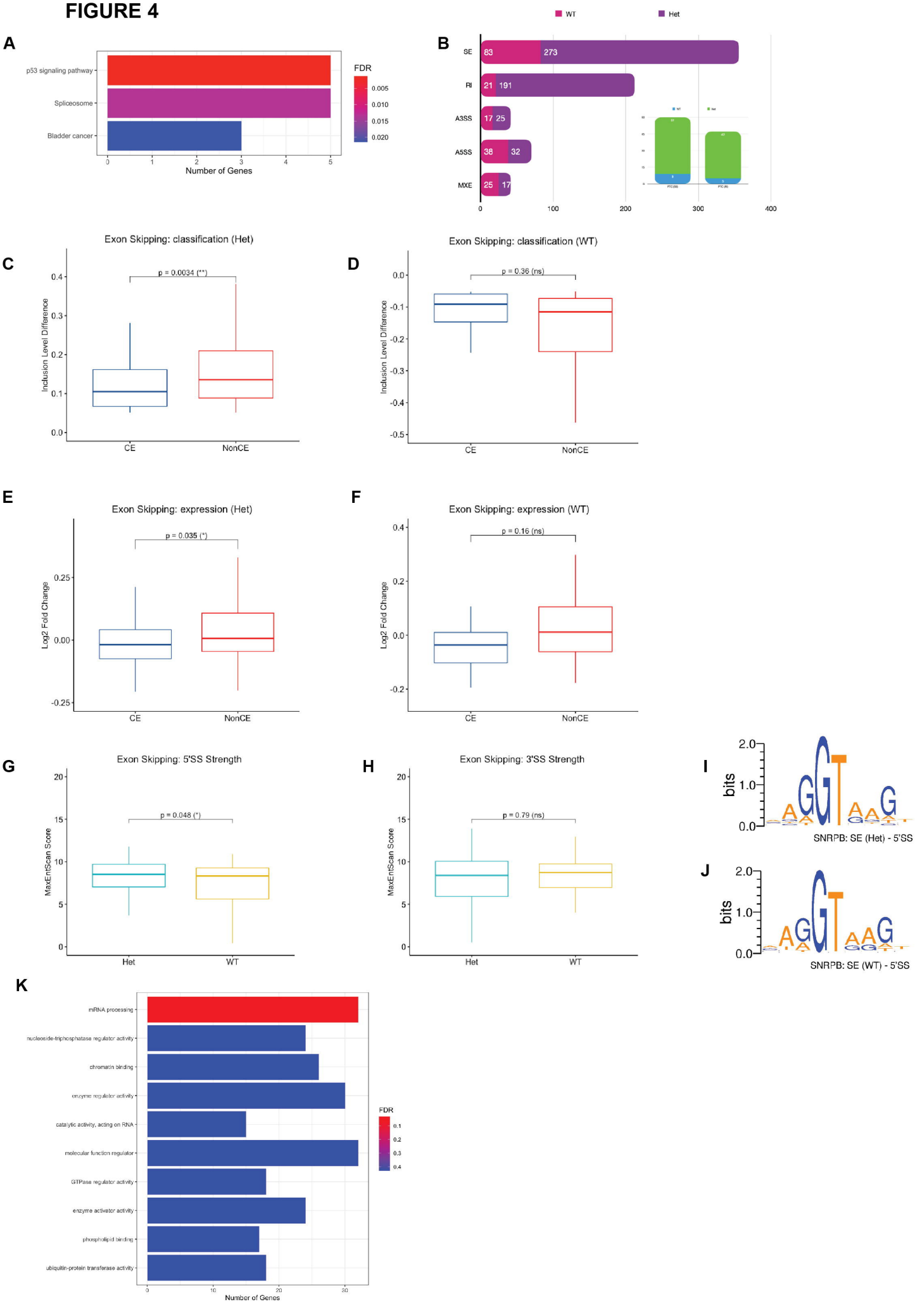
A
p53 signaling pathway
Spliceosome
Bladder cancer
Number of Genes
FDR
0.005
0.010
0.015
0.020
B
WT
Het
SE
RI
A3SS
A5SS
MXE
83
273
21
191
17
25
38
32
25
17
C
Exon Skipping: classification (Het)
p = 0.0034 (**)
Inclusion Level Difference
CE
NonCE
D
Exon Skipping: classification (WT)
p = 0.36 (ns)
Inclusion Level Difference
CE
NonCE
E
Exon Skipping: expression (Het)
p = 0.035 (*)
Log2 Fold Change
CE
NonCE
F
Exon Skipping: expression (WT)
p = 0.16 (ns)
Log2 Fold Change
CE
NonCE
G
Exon Skipping: 5'SS Strength
p = 0.048 (*)
MaxEntScan Score
Het
WT
H
Exon Skipping: 3'SS Strength
p = 0.79 (ns)
MaxEntScan Score
Het
WT
I
bits
SNRPB: SE (Het) - 5'SS
J
bits
SNRPB: SE (WT) - 5'SS
K
mRNA processing
nucleoside-triphosphatase regulator activity
chromatin binding
enzymic regulator activity
catalytic activity, acting on RNA
molecular function regulator
GTPase regulator activity
enzyme activator activity
phospholipid binding
ubiquitin-protein transferase activity
Number of Genes
FDR
0.1
0.2
0.3
0.4

FIGURE 5

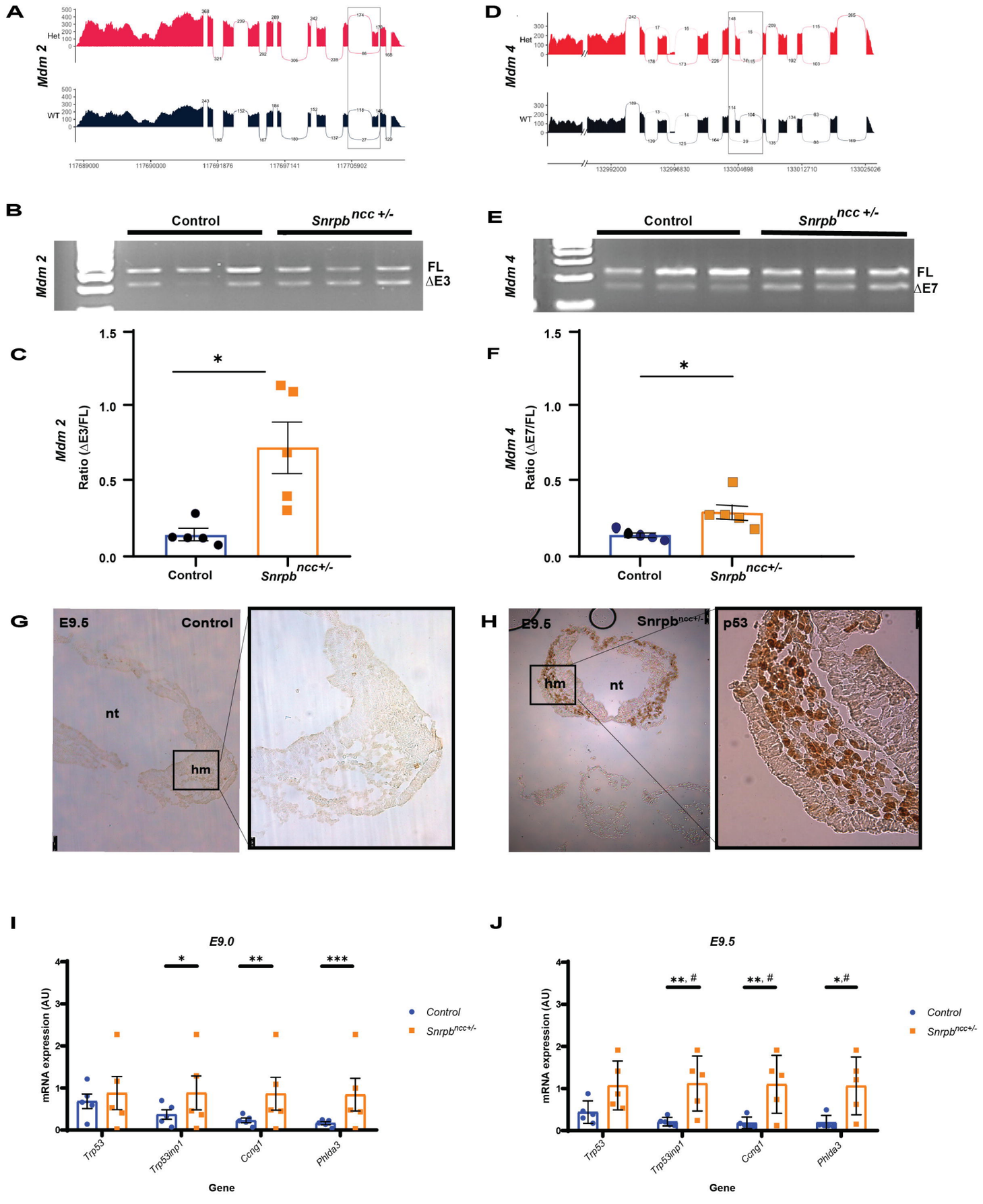
A
Mdm 2
Het
WT
117689000
117690000
117691876
117697141
117705902
D
Mdm 4
Het
WT
132992000
132996830
133004898
133012710
133025026
B
Control
Snrpb ncc +/-
Mdm 2
FL
ΔE3
E
Control
Snrpb ncc +/-
Mdm 4
FL
ΔE7
C
Mdm 2
Ratio (ΔE3/FL)
1.5
1.0
0.5
0.0
*
Control
Snrpb ncc+/-
F
Mdm 4
Ratio (ΔE7/FL)
1.5
1.0
0.5
0.0
*
Control
Snrpb ncc+/-
G
E9.5
Control
nt
hm
H
E9.5
Snrpb ncc+/-
hm
nt
p53
I
E9.0
mRNA expression (AU)
*
**
***
Control
Snrpb ncc+/-
Trp53
Trp53inp1
Ccng1
Phida3
Gene
J
E9.5
mRNA expression (AU)
**, #
**, #
*,#
Control
Snrpb ncc+/-
Trp53
Trp53inp1
Ccng1
Phida3
Gene

FIGURE 6

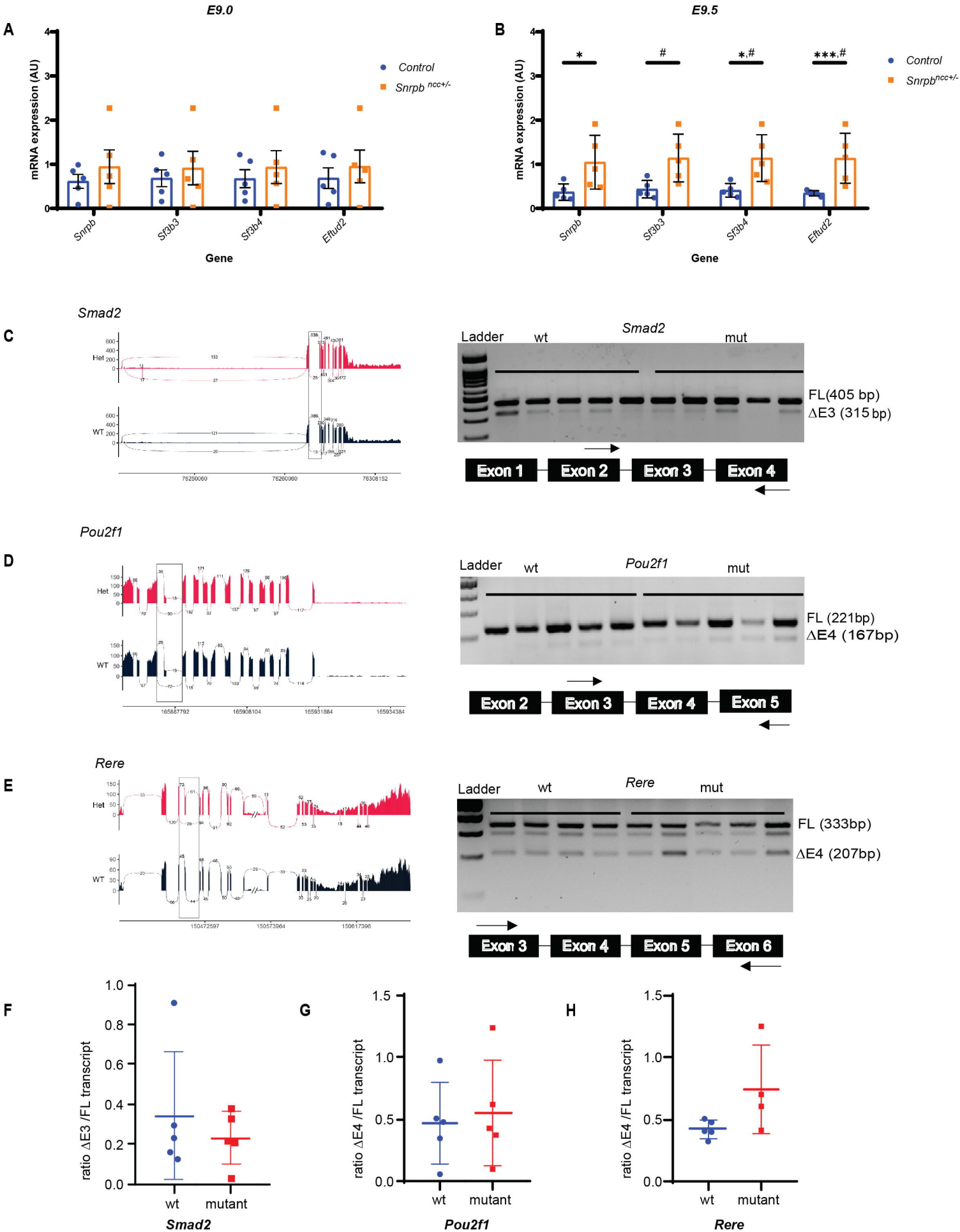
A
E9.0
mRNA expression (AU)
Control
Snrpb ncc+/-
Snrpb
Sf3b3
Sf3b4
Eftud2
Gene
B
E9.5
*
#
*,#
***,#
C
Smad2
Ladder
wt
mut
FL(405 bp)
ΔE3 (315 bp)
Exon 1
Exon 2
Exon 3
Exon 4
D
Pou2f1
FL (221bp)
ΔE4 (167bp)
Exon 5
E
Rere
FL (333bp)
ΔE4 (207bp)
Exon 6
F
ratio ΔE3 /FL transcript
G
ratio ΔE4 /FL transcript
H